FRACTURE TOUGHNESS CHARACTERIZATION OF THERMOSETTING POLYMER SYSTEMS REINFORCED BY GRAPHENE NANOPLATELETS

By

Abdulrahman Alfadhli

A THESIS

Submitted to
Michigan State University
in partial fulfillment of the requirements
for the degree of

Mechanical Engineering — Master of Science

2020

ABSTRACT

FRACTURE TOUGHNESS CHARACTERIZATION OF THERMOSETTING POLYMER SYSTEMS REINFORCED BY GRAPHENE NANOPLATELETS

By

Abdulrahman Alfadhli

The interlaminar fracture toughness is a critical property for the damage tolerance, impact resistance, and delamination of fiber-reinforced polymer (FRP) composites. To enhance this property, various strategies have been explored, from introducing through the thickness reinforcement, strengthening the fiber-matrix interface, to improving the fracture toughness of the matrix resins. This research examines the effects of Graphene Nanoplatelet (xGnP) on the fracture toughness of epoxy resins commonly used in FRPs. Two epoxy systems were examined: EPON 862 and SC-15. xGnP was added into the epoxy resins at two weight fractions: 0.1wt% and 0.5wt%. The fracture toughness of the reinforced resins was investigated with the compact tension (CT) experiment. It was observed that xGnP resulted in a greater enhancement in the fracture toughness of EPON 862 than that of SC-15. For EPON 862, the G_{IC} value had an improvement of 87% and 156% for the reinforced 0.1wt% and 0.5wt%, respectively. For SC-15, the improvement was 21% and 14% for the reinforced 0.1wt% and 0.5wt%, respectively. SC-15 is already rubber toughened. For comparison purpose, EPON 862 was also reinforced with nano-silica particles. At 0.1wt% and 0.5wt%, the improvement in G_{IC} was 49% and 87%, respectively. In summary, adding xGnP can significantly improve the fracture toughness of a relatively brittle epoxy system. At a low concentration, xGnP is much more efficient than nano-silica in terms of improving the fracture toughness. Finally, in fracture experiment, the method of introducing pre-crack was found to have a significant effect on the measured fracture toughness value.

ACKNOWLEDGMENTS

I would like to express my deepest appreciation to my advisor Dr. Xinran Xiao for her support, encouragement, and guidance during my graduate study. The professor has taught me how to review literature papers and how to form a research plan. Without her assistance, I would never be able to accomplish this thesis. Dr. Xiao was always available and willing to give above and beyond to help me with the research. I also would like to acknowledge Dr. Shiwang Cheng for his contribution. His contribution by providing the material with the nano additives was precious. I am thankful to Dr. Patrick Kwon for accepting to be a member of the master thesis committee. I am also grateful to all my colleagues for their continuous support and help, including Sakib Iqbal, Shutian Yan, Royal Ihuaenyi, Jie Fu, and Ru Tao.

I want to show gratitude to my parents, who sacrificed to raise and educate me. Without their inspiration, guidance, and support, I might not be the person I am today. I am deeply thankful to my wife for her continuous support and encouragement. Without her, I would never be able to continue my graduate studies. I appreciate my brothers, sisters, and friends for their great motivation. Finally, I would like to thank the Kingdom of Saudi Arabia and The Islamic University of Madinah for the fellowship to pursue my higher education.

TABLE OF CONTENTS

LIST OF TABLES . . . . . **vi**

LIST OF FIGURES . . . . . **vii**

KEY TO SYMBOLS . . . . . **x**

Chapter 1 Introduction and Literature Review **1**
1.1 Thesis Organization 1
1.2 Introduction 2
1.3 Graphene-based Nanocomposites 3
1.3.1 Toughening Mechanisms 5
1.3.2 Dispersion of Nanofillers 6
1.4 Fracture Mechanics 7
1.4.1 Types of Fracture. 8
1.4.2 Modes of fracture 9
1.4.3 Linear-Elastic Fracture Mechanics (LEFM) 9
1.4.3.1 Griffith's Energy Balance Criteria 10
1.4.3.2 Stress Intensity Factor (K) 11
1.4.3.3 Relationship Between Energy Release Rate and Stress Intensity Factor 13
1.4.4 Elastic-Plastic Fracture Mechanics (EPFM) 13
1.4.4.1 Crack tip opening displacement (CTOD) 13
1.4.4.2 J-integral 14

Chapter 2 Fracture Toughness Experiment **15**
2.1 Testing Standards and Calculations 15
2.2 Materials and Methods 18
2.2.1 Curing Cycle and Specimen Preparation 19
2.3 Experiment Setup 22
2.4 Data Acquisition 24

Chapter 3 Results and Dissection **26**
3.1 Different Pre-cracking Procedures and their Effects 26
3.2 Fracture toughness Results 30
3.2.1 EPON 862 30
3.2.2 SC-15 33
3.3 Stress Distribution and Plasticity Correction 35
3.3.1 Creager and Paris (1967)'s Estimation 43
3.3.2 Stress Distribution for Diffident Samples' Loading 44
3.3.3 Plastic Zone Shape 45

Chapter 4 Conclusion **48**
4.1 Summary and Conclusion 48
4.2 Future Work 49

APPENDIX **50**

BIBLIOGRAPHY **54**

LIST OF TABLES

Table 3.1: Comparison between two different pre-cracking methods on EPON 862's fracture toughness 28

Table 3.2: Comparison between two different pre-cracking methods on SC-15's fracture toughness 28

Table 3.3: K_{IC} $(MPa.\sqrt{m})$ averages of EPON 862 with xGnP 31

Table 3.4: G_{IC} (J/m^2) averages of EPON 862 with xGnP 31

Table 3.5: K_{IC} $(MPa.\sqrt{m})$ averages of EPON 862 with Nano-silica 32

Table 3.6: G_{IC} (J/m^2) averages of EPON 862 with Nano-silica 32

Table 3.7: K_{IC} $(MPa.\sqrt{m})$ averages of SC-15 with xGnP 35

Table 3.8: G_{IC} (J/m^2) averages of SC-15 with xGnP 35

Table 3.9: Mechanical Property of SC-15 baseline. 38

Table 3.10: The three example samples of SC-15 with 0.5wt% xGnP. 39

Table A.1: SC-15 Samples - baseline. 51

Table A.2: SC-15 Samples - 0.1wt% xGnP. 51

Table A.3: SC-15 Samples - 0.5wt% xGnP. 51

Table A.4: EPON 862 Samples - baseline. 52

Table A.5: EPON 862 Samples - 0.1wt% xGnP. 52

Table A.6: EPON 862 Samples - 0.5wt% xGnP. 52

Table A.7: EPON 862 Samples - 0.1wt% Nano-Silica. 52

Table A.8: EPON 862 Samples - 0.5wt% Nano-Silica. 53

LIST OF FIGURES

Figure 1.1: Mode-I interlaminar fracture toughness of composites G_{IC}^{c} and mode-I matrix toughness G_{IC}^{m} for conventional composites [1]. 3

Figure 1.2: Maps of different mechanical properties for nanocomposites with respect to particle loading: (a) Fracture toughness map. (b) Stiffness map. (c) Ultimate tensile strength map. Obtained from [2]. 4

Figure 1.3: Modes of fracture: Mode I Opening, Mode II In-plane shear, Mode III Out-of-plane share, Drawing obtained from [3]. 9

Figure 1.4: An infinite wide plate with a through thickness ellipse crack subjected to remote tensile stress, Drawing obtained from [4]. 11

Figure 1.5: Polar coordinates of the stresses ahead of the crack tip. Drawing obtained from [4]. 12

Figure 2.1: The ASTM D5045 standard [5]: (a) Specimen configurations. (b) Load vs loading point displacement curve. 16

Figure 2.2: Solvent evaporation process. 20

Figure 2.3: Sample's design and silicon molds: (a) The design the stainless steel prototype in (mm) following the standards [5]. (b) The stainless steel prototype and the silicon mold. 21

Figure 2.4: After completing the curing cycle: (a) Samples lift inside the open door oven to cool down after finishing the curing cycle. (b) Samples are ready to be carefully extracted from the molds. 21

Figure 2.5: SC-15 samples, from right: baseline, 0.1wt%, then 0.5wt% of xGnP. . . . 22

Figure 2.6: EPON 862 samples: (a) 0.1wt%,0.5wt% of nano-silica. (b) 0.1wt%,0.5wt% of xGnP. (c) Baseline. 22

Figure 2.7: The experiment setup with camera and light source. 23

Figure 2.8: Samples arrangement before attaching to the tensile grip: (a) Front view. (b) Side view. 24

Figure 2.9: The experiment's stages until the fracture: (a) The second still image. (b) The middle of the test. (c) The moment before the fracture. (d) The moment after the fracture. 25

Figure 3.1: The two methods of pre-cracking: (a) Pressing the razor into the notch. (b) Sliding the razor on the notch. 27

Figure 3.2: The strain field of the pressed sample: (a) Before inserting the blade. (b) ϵ_x after inserting the blade. (c) ϵ_y after inserting the blade. 29

Figure 3.3: Load vs Loading-point displacement of EPON 862 with xGnP. 30

Figure 3.4: K_{IC} and G_{IC} of EPON 862 with xGnP. 31

Figure 3.5: Comparison between EPON 862 with xGnP and EPON 862 with Nano-Silica for different weight fractions. 32

Figure 3.6: Load vs Loading-point displacement of SC-15 with xGnP. 33

Figure 3.7: K_{IC} and G_{IC} of SC-15 with xGnP. 34

Figure 3.8: The stress field near the crack tip. 35

Figure 3.9: First-order and second-order estimates of plastic zone size (r_y and r_p, respectively). The cross-hatched area represents the load that must be redistributed, resulting in a larger plastic zone. Obtained from [6]. 37

Figure 3.10: The first specimen's normal stress σ_y distribution along the crack path just before the fracture. 40

Figure 3.11: The second specimen's normal stress σ_y distribution along the crack path just before the fracture. 40

Figure 3.12: The third specimen's normal stress σ_y distribution along the crack path just before the fracture. 41

Figure 3.13: Load vs CTOD for the three samples. 42

Figure 3.14: Comparison between Irwin's modification and Creager and Paris's estimation. 44

Figure 3.15: The normal stress σ_y distribution along the crack path for different loading. 45

Figure 3.16: The plastic zone shape estimation from the elastic solution for Mode I. Obtained from [6]. 46

Figure 3.17: The effective stress from a finite element analysis Vs the plastic zone estimation [6]. 46

Figure 3.18: Strain distribution of y-direction. 47

Figure A.1: Compact tension specimen configuration. 51

Figure A.2: Microscopic image of a crack tip made by razor sliding. 53

Figure A.3: Microscopic image of a crack tip made by razor pressing. 53

KEY TO SYMBOLS

FRP	Fiber-reinforced Polymer
xGnP	Graphene nanoplatele
CNTs	Carbon nanotubes
K_{IC}	Mode I Critical Stress Intensity Factor
G_{IC}	Mode I Critical Strain Energy Release Rate
CTOD	Crack Tip Opening Displacement
J	J-integral
LEFM	Linear Elastic Fracture Mechanic
EPFM	Elastic-Plastic Fracture Mechanics
T	Temperature
T_g	Glass Transition Temperature
SSY	Small Scale Yielding
EDM	Electrical Discharge Machining
CT	Compact Tension
SENB	Single Edge Notched Bend
P	Load
B	Thickness
W	Width
a	Crack Length
DIC	Digital Image Correlation
FEA	Finite Element Analysis
SEM	The Standard Error of the Mean

Chapter 1: Introduction and Literature Review

1.1 Thesis Organization

This thesis is structured as follows:

Chapter 1 reviews the relationship between the fracture toughness of the matrix and the interlaminar fracture toughness of the fiber-reinforced polymer. This chapter overviews the literature on the mechanical effects of adding nanofillers to epoxy resins. The reasons for choosing the graphene nanoplatelets as an additive are discussed. Since the focus is on the fracture toughness property, fracture mechanics and fracture toughness are explained in this chapter.

Chapter 2 discusses the methodology of the study, from identifying the standards, preparing the material, to manufacturing the specimens. The testing procedure and the data acquisition method are described.

Chapter 3 reports the findings of both epoxy systems and evaluates the influence of adding nano additives. The last part of this chapter presents analytical solutions for the stress distribution along the crack path and the crack-tip plasticity. Furthermore, a comparison between the analytical solutions and the experimental analysis is presented.

Chapter 4 summarizes and concludes the thesis in addition to recommending future work.

1.2 Introduction

The interlaminar fracture toughness is a key property for the damage tolerance and impact resistance of fiber-reinforced polymer (FRP) composites [7–10]. To improve this property, various strategies have been explored, from introducing through the thickness reinforcement, increasing the fiber/matrix interface strength, to enhancing the toughness of the matrix resins. Each method has led to some improvement, but the problem is far from being solved. This thesis focuses on investigating the enforcement of the matrix by graphene nanoplatelets as the correlation between composites' and matrices' fracture toughness is evident.

The matrix toughness is one of the dominant factors determining the interlaminar fracture toughness of composites duo to the interaction between the nanoparticles and the reinforcing fibres [1, 10, 11]. To improve the matrix resin toughness, various strategies have been developed, including rubber toughened thermoset resins and thermoplastic resins. The matrix toughening efficiency is gauged by the $G^c_{\mathrm{IC}}/G^m_{\mathrm{IC}}$ ratio, i.e. The Mode-I interlaminar fracture toughness of the composite over the Mode-I fracture toughness of the matrix resin. Improving the matrix toughness is particular efficient for brittle resin systems. A general trend is $G^c_{\mathrm{IC}}/G^m_{\mathrm{IC}} > 1$ for brittle matrices when $G^m_{\mathrm{IC}} < 500 J/m^2$, and $G^c_{\mathrm{IC}}/G^m_{\mathrm{IC}} < 1$ for tough matrices when $G^m_{\mathrm{IC}} > 500 J/m^2$ in conventional fiber-reinforced polymers (FRP)s, as shown in Figure 1.1. It was found that the higher amount of nanoparticles dispersed into the resin, the lower matrix toughening efficiency $G^c_{\mathrm{IC}}/G^m_{\mathrm{IC}}$ observed [11].

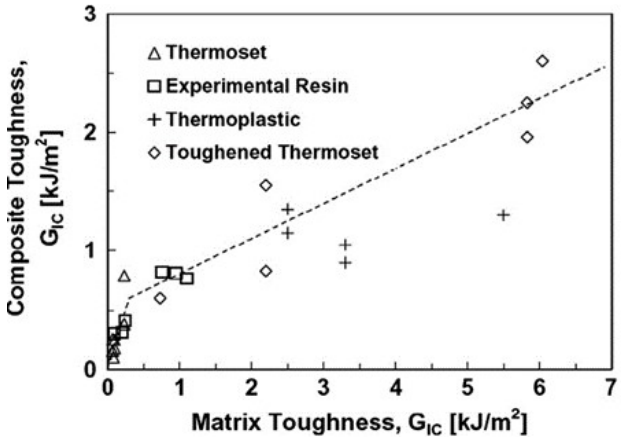

Figure 1.1: Mode-I interlaminar fracture toughness of composites G_{IC}^{c} and mode-I matrix toughness G_{IC}^{m} for conventional composites [1].

1.3 Graphene-based Nanocomposites

The fracture toughness and strength are two fundamental properties for structural material. Usually, they are not compatible. The improvement of one is often at the expense of the other. The emerging nanocomposite has changed this perspective. With the addition of nano-sized fillers, polymers can be tougher, stronger, and with added multi-functionality. Among them, graphene appears to have the highest efficiency at the low filler loading region.

It is not a simple task to compare the efficiency of different nanofillers due to the diversity in materials source, the wide range of dispersion methods, and the sizes of these fillers. By compiling data from hundreds of research papers on epoxy-based nanocomposites, Domun et al. [2] generated a set of maps that compare the efficiency of four types of nanoparticles on fracture toughness, stiffness, and strength, as shown in Figure 1.2. In these maps, The properties are given as the ratio to the neat epoxy, and the data points above 1.0 line indicate a positive effect. The Figures compare the efficiency of nanoparticles/epoxy nanocomposites (with Carbon nanotubes, graphene, nanoclay and nanosilicon) with respect to particle loading weight fraction [2].

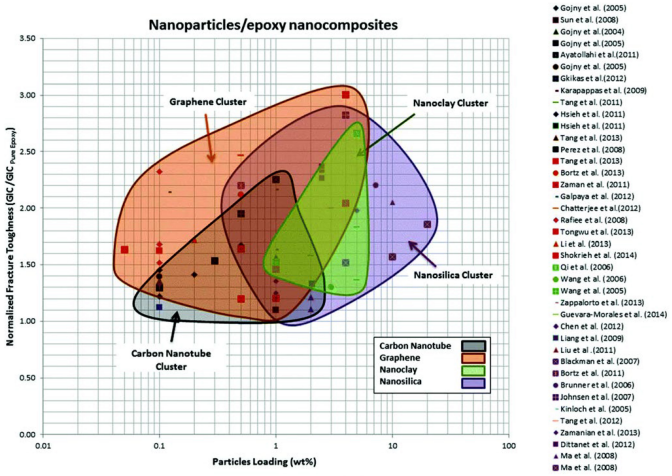

(a)

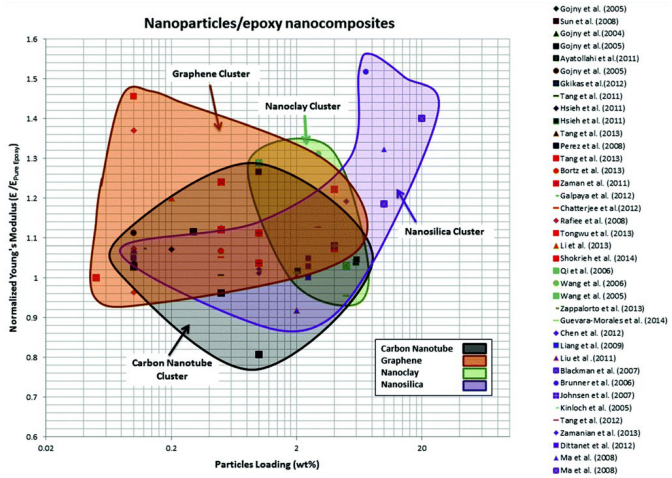

(b)

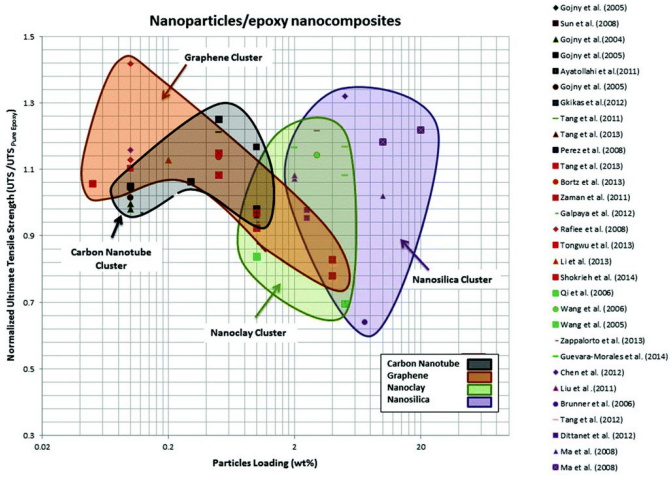

(c)

Figure 1.2: Maps of different mechanical properties for nanocomposites with respect to particle loading: (a) Fracture toughness map. (b) Stiffness map. (c) Ultimate tensile strength map. Obtained from [2].

Figures 1.2 shows that the graphene is a clear winner in the region of low weight fraction up to 0.5wt%. Graphene consistently out-performed carbon nanotubes (CNTs), nanoclay and nanosilica in all three properties. This confirms the earlier findings of Rafiee et al. [12] that at a low concentration of 0.1wt%, graphene nanoplatelet (GNP)/epoxy out performed SWCNT/epoxy and MWCNT/epoxy nanocomposites by a significant margin in tensile modulus, strength, Mode-I fracture toughness, and fatigue cracking resistance.

1.3.1 Toughening Mechanisms

The remarkable toughening effect of nanofillers has been attributed to additional toughening mechanisms brought upon by these fillers [11]. For 0-D and 1-D fillers, these include greater energy absorption from filler/matrix resin debonding and/or nanotube pull-out due to the extraordinarily large interface area, reduced plastic zone due to increased matrix yield stress, and higher matrix/fiber interfacial strength. In nanoclay composites, it was observed that the platelets produce nanovoids/cracks and promote shear yielding of the matrix at the crack tip.

The mechanics of graphene nanocomposites have been discussed by Young et al. [13]. In a graphene sheet, the carbon atoms are held together by sp^2 bonds, which render the graphene with ultra-high in-plane stiffness, strength, and conductivity. The bonds between sheet layers are weak van der Waals forces. The interfacial shear strength between the graphene sheets was found to be at the order of 1MPa. For in-plane modulus of elasticity, Lee at al. [14] measurement for the monolayer graphene membrane was about 1TPa. How this unique structure links to its reinforcing effect in nano and multiscale composites is yet to be understood. The above findings suggest that further research is needed to explore the potential of using graphene-modified resins in improving the interlaminar fracture toughness

and impact resistance of structural composites.

1.3.2 Dispersion of Nanofillers

One of the most critical steps in preparing high-quality graphene-based epoxy composites is the method of nano-graphene dispersion. Improper distribution of the graphene into the epoxy may cause issues such as void formation, insufficient curing of the epoxy, viscosity buildup of the epoxy, and shear thinning [15]. The optimal method of graphene dispersion will help to get higher mechanical bonding between the epoxy and the nano-graphene platelets (NGP) and enhance material performance [15].

Solution mixing and high shear mixing are two of the most commonly used methods for dispersing nano-graphene platelets (NGP) into the polymer [15]. Solution mixing uses the sonication process to disperse the NGPs into a proper organic solvent flowing by adding the epoxy and then evaporate the solvent [16, 17]. High shear mixing mechanically distribute the NGPs into the polymer [18,19]. Kumar [18] used only a high shear mixer at 2000 rpm to disperse the NGPs into the epoxy following notes from the NGP manufacturer, and reported good dispersion quality and random orientation. However, at higher weight fraction, some agglomeration of the graphene platelets have occurred. Kumar in 2018 [19], following Yang's paper [20] suggestions, hydrogen passivated the NGPs using 5% H2/N2 mixture to improve dispersion of the platelets then used a high shear mixer to disperse HP-NGPs into the epoxy. Kumar using an optical microscope compared passivated and non-passivated NGPs composites and showed the benefits of the hydrogen passivation on the dispersion of the NGPs.

Rafiee [16] dispersed GPL into acetone using high amplitude ultrasonic then added the epoxy flowing the same procedure. The acetone later was removed through heating the mix-

ture. Wajid [17] prepared the graphene-based epoxy composites using two techniques: solution processing and freeze-drying and compared between them. Wajid for the first method used DMF as a solvent for PVP-stabilized graphene before adding the epoxy. DMF was chosen because they found it to be the best compatibility with their epoxy resin. After adding the epoxy, the solution was tip sonicated to ensure the uniform dispersion of the graphene "less agglomeration". Then, the DMF was evaporated by heating the mixture while magnetically mix the solution to ensure the uniform distribution of the epoxy in the mixture. To ensure the elimination of the remaining solvent, the solution was placed in a vacuum oven at a specified temperature for 14 h. The other method is freeze-drying. The polymer-stabilized graphene in water were freeze-dried using a Vitris Benchtop Freeze Dryer throughout 48 h to obtain a dark gray colored powder. The freeze-dried PVP-stabilized graphene was redispersed in the resin by stirring and sonicating for 30min. The hardener was added to the graphene/resin mixture and was cured under the same conditions as the solution processing method. Wajid [17] concludes that the solution processing method results in reliable dispersion quality but suffers from residual solvent at high-graphene concentrations, unlike the solvent-free technique, freeze-dry mixing, that avoids this problem.

1.4 Fracture Mechanics

It is often assumed during the design process that the material is isotropic and flawless. However, this is almost impossible to achieve, as microstructure and other scales defects are usually inevitable during the manufacturing process. If the existence of cracks is not taken into account during design, these flows can cause severe consequences. These defects can lead to a complete failure of the system even though the total stress is way below the

ultimate tensile strength of the material. Many accidents occurred in history due to a lack of consideration of fracture mechanics, which is the theoretical explanation of the cracks' behavior in materials. If the concept of fracture mechanics is appropriately applied, most of these incidents could be avoided.

Fracture toughness is the study of the material's resistance to crack propagation and described by several parameters; stress intensity factor (K), energy release rate (G), J-integral (J), and crack tip opening displacement (CTOD). Tensile properties, crack geometry, and temperature are factors affecting the fracture toughness of the material. Epoxy resins can fracture either in the linear elastic or nonlinear elastic-plastic regimes. There are two main approaches to describe the fracture mechanics; Linear Elastic Fracture Mechanics (LEFM) and Elastic-Plastic Fracture Mechanics (EPFM). Epoxies often obey (LEFM) when they are well below their glass transition temperature T_g and obey (EPFM) when they are near and above their T_g.

1.4.1 Types of Fracture.

There are mainly two types of fracture: brittle fracture and ductile fracture. Brittle fracture corresponds to the sudden and rapid crack propagation under stress, where the material exhibited little or no plastic deformation prior to failure. Consequently, a relatively small amount of energy is required to complete the fracture. On the other hand, ductile fracture occurs when the crack has a substantial plastic deformation before separation, and this usually takes longer time and required more energy [4].

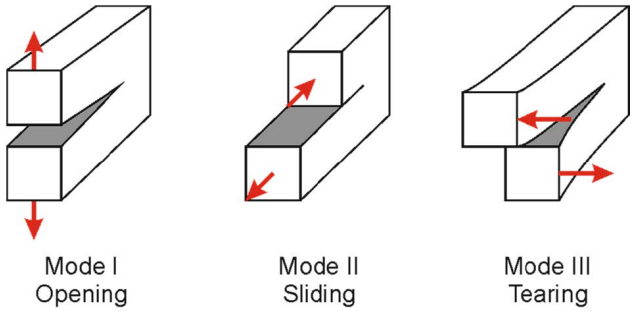

Figure 1.3: Modes of fracture: Mode I Opening, Mode II In-plane shear, Mode III Out-of-plane share, Drawing obtained from [3].

1.4.2 Modes of fracture

There are three basic modes of fracture indicated in Figure 1.3. In a real situation, materials and cracks could experience a combination of two or all three styles. Mode I has the load perpendicular to the crack surface, and this mode requires low load and energy to propagate the crack compared to the other two modes. Mode I loading is the most common mode used for fracture toughness characterization. Mode II loading experiences in-plane shearing stress and Mode III experiences out-of-plane shearing stress.

1.4.3 Linear-Elastic Fracture Mechanics (LEFM)

Linear elastic fracture mechanics (LEFM) is a theory based on Griffith's criteria and describes the experienced stress at cracks within the yield limit. This theory describes the deformation in the elastic region for materials that obey Hooke's law of linear elasticity. However, small scale yielding (SSY) mostly occurs, and it is generally neglectable. LEFM has two parameters for the fracture toughness: Energy release rate (G) and Stress intensity factor (K).

1.4.3.1 Griffith's Energy Balance Criteria

An English aeronautical engineer A.A. Griffith in the 1920s [21] has led one of the well-known early advances of fracture mechanics where he studied brittle fracture on glass. Following the principle of the first law of thermodynamics, the assumption was that the overall energy experienced by the crack would be in equilibrium with the load applied to the crack. Therefore, there is no change in total energy under equilibrium until the crack hits the critical stage and start growing. When the crack progresses, it releases energy, so the energy that is applied to the crack and the energy received by the crack is no longer in equilibrium, and there will be a net decrease of energy. For the crack to expand, there must be enough potential energy to surmount the surface energy. For an infinite wide plate with a through-thickness crack subjected to tensile stress in-plane stress condition as shown in Figure 1.4, The Griffith energy balance for growth in the crack area dA is expressed in equilibrium conditions as in Eq.1.1. Where Π is the potential energy supplied by the internal strain energy and external stress, and W_s is the work needed to create new surfaces. After development by Griffith's (1921) based on the analysis of Inglis [22], the fracture stress, σ_f is obtained as in Eq.1.2 for isotropic linear elastic materials where γ_s is the surface energy of the material.

$$\frac{d\Pi}{dA} + \frac{dW_s}{dA} = 0 \tag{1.1}$$

$$\sigma_f = \sqrt{\frac{2\gamma_s E}{\pi a}} \tag{1.2}$$

In 1956, Irwin [23] introduced a fracture energy solution that is basically similar to Griffith's concept, except that Irwin's approach is in shape more practical to address engineering

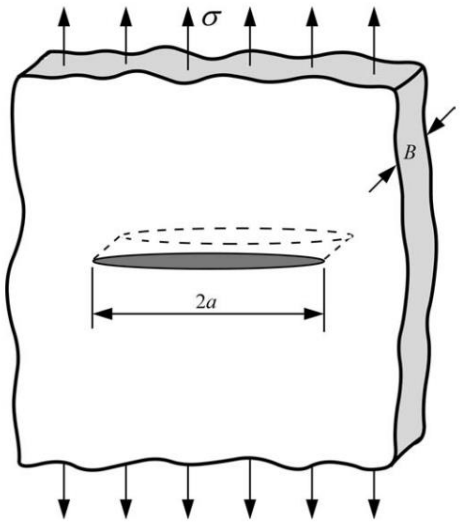

Figure 1.4: An infinite wide plate with a through thickness ellipse crack subjected to remote tensile stress, Drawing obtained from [4].

challenges. Irwin defines the energy release rate G which is the measurement of the available energy for a crack extension, as the rate of change in potential energy with the crack area. Irwin [23] describes the released energy duo to the crack initiations in Eq.1.3. Where Π is the potential energy of the crack, which is also known as the crack extension force, and A is the crack area.

$$G = -\frac{d\Pi}{dA} \tag{1.3}$$

1.4.3.2 Stress Intensity Factor (K)

Westergaard [24], Irwin [25], et al. are the first to drive expressions describing the stress field near the crack tip for a cracked body with external force considering the isotropic behavior of linear elastic materials. The first order stress field could be defined in a linear isotropic material, setting the crack tip as the origin of the polar coordinate axis, as shown in Figure 1.5 and expressed in Eq.1.4. Where σ_{ij} is the stress tensor, K is the stress intensity factor,

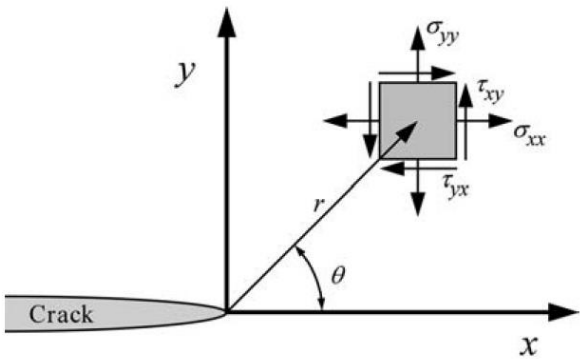

Figure 1.5: Polar coordinates of the stresses ahead of the crack tip. Drawing obtained from [4].

and f_{ij} is a dimensionless function, while r and θ are polar the coordinates.

$$\sigma_{ij} = \left(\frac{K}{\sqrt{2\pi r}}\right) f_{ij}(\theta) + \cdots \tag{1.4}$$

Stress intensity factor K is a parameter introduced by Irwin [25] used in LEFM to predict the stress state near the crack tip. A subscript is assigned to the stress intensity factor to denote the loading mode, that is, K_I, K_{II}, or K_{III}. Eq.1.5 is to determine K_I of the field stresses in the vicinity of the crack tip. Where Y is a dimensionless factor depends on crack geometry and loading condition, σ is the applied load, and a is the crack length. Y in the case of fracture toughness test described as a function of crack to width ratio a/W as in Eq.1.6.

$$K_I = Y\sigma\sqrt{\pi a} \tag{1.5}$$

$$K_I = \frac{P}{B\sqrt{W}}\, f\left(\frac{a}{W}\right) \tag{1.6}$$

1.4.3.3 Relationship Between Energy Release Rate and Stress Intensity Factor

Energy release rate G and Stress intensity factor K are two different parameters describing cracks. G is a parameter based on the strain energy, and K is based on the stress near the crack tip. Considering the two Equations in 1.7, a relationship between the two parameters can be described for plane strain conditions as in Eq.1.8.

$$\begin{aligned} G &= \frac{\pi\sigma^2 a}{E} \\ K_I &= \sigma\sqrt{\pi\ a} \end{aligned} \tag{1.7}$$

$$G = \frac{K^2\left(1-v^2\right)}{E} \tag{1.8}$$

1.4.4 Elastic-Plastic Fracture Mechanics (EPFM)

The previous two parameters, the energy release rate and stress intensity factor don't describe the material that exhibiting a significant plastic deformation at the crack tip and would deform plastically after reaching the maximum stress. Two new parameters would be introduced for this type of materials: Crack tip opening displacement (CTOD) and J-integral.

1.4.4.1 Crack tip opening displacement (CTOD)

A fracture criterion known as crack tip opening displacement was introduced by Wells [26] that measures the physical opening of the crack tip. CTOD is the distance of the opening of an initial crack tip to the point of stable or unstable crack extension in a typical fracture toughness test specimen. The maximum crack tip opening due to cleavage cracking or plastic failure is the CTOD. Materials that showing elastic-plastic behavior before fracture would

experience plastic deformation at the crack tip.

1.4.4.2 J-integral

Rice [27] proposed the J-integral energy approach, which is based on the density of the strain energy around the crack tip. J-integral describes the independent crack path of strain energy release rate, applicable to both linear and nonlinear elastic material. The J-integral would have a constant value characterizing the stress and strain field in the vicinity of the crack tip. In LEFM, G is assumed to be the available energy to extend the crack, which is equal to J. However, for an elastic-plastic material, part of the energy is used in plastic deformation as the crack propagates.

Chapter 2: Fracture Toughness Experiment

The methodology of this study is described in this chapter as follows. Since the base of this thesis is the fracture experiment, the first section identified the standards that were adapted for testing, from designing the samples, performing the test, to calculating the properties. Preparing the material and manufacturing the specimens took a decent amount of the chapter due to its significant role in final results. Before moving on to the next chapter that discussing the results, detailed information was included about the testing procedure and data acquisition.

2.1 Testing Standards and Calculations

The mode I plane strain fracture toughness test for plastic materials follows The ASTM D5045 standard to determine the critical stress intensity factor K_{IC}, and the energy per unit area of crack surface or critical strain energy release rate G_{IC}. ASTM E399 for metallic materials with brittle fracture is used for more details and requirements. The standard permits two different specimen shapes: single edge notched bend (SENB) and compact tension configuration (CT) shown in Figure 2.1(a). The compact tension configuration (CT) has been selected for this research. The standard indicates that three measurements are necessary for K_{IC} and G_{IC} calculations: the thickness B, the crack length a, and the width W. The recommended testing condition for the temperature is 23 °C, and the cross-head displacement rate to be (10 mm/min). The loading times shouldn't be less than 1 ms because the risk of dynamic effects causing errors. The standard requires at least three replicate tests for each material condition and accurate integration of the load versa loading point

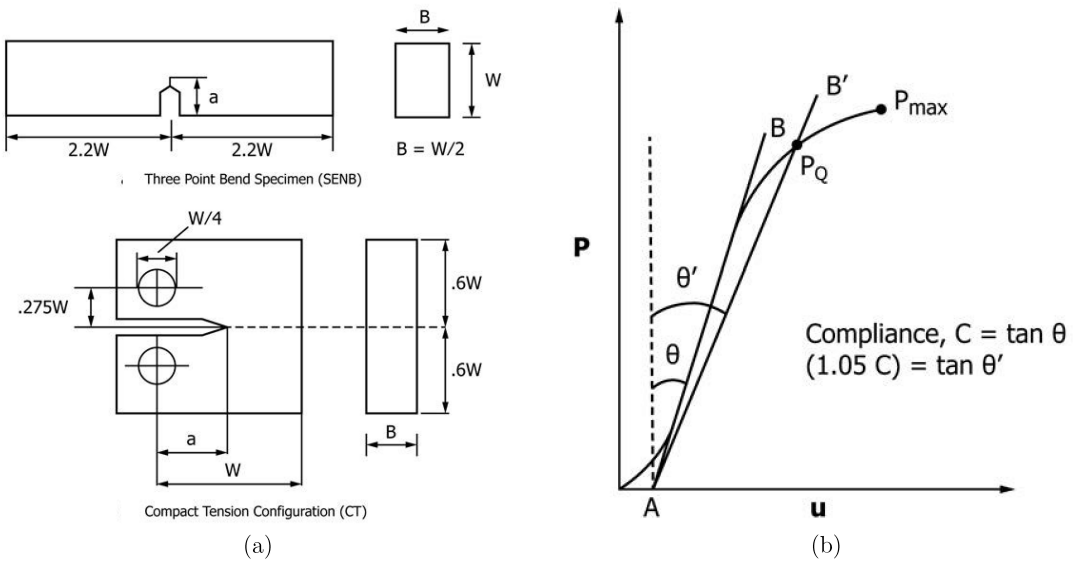

Figure 2.1: The ASTM D5045 standard [5]: (a) Specimen configurations. (b) Load vs loading point displacement curve.

displacement, which is used to determine accurate results of critical strain energy release rate G_{IC}. The ideal case of the test is a linear diagram with a sudden drop of the load at the instant of crack initiation [5].

For pre-cracking, the standard ASTM D5045 recommends the natural crack to be made by sawing or tapping a fresh razor blade. The length of the pre-crack should be at least twice longer than the width of the sawed-in slot or the tip radius of the machined notch. If the pre-crack cannot be generated by tapping the razor because of the material brittleness, sliding the razor blade across the machined groove is the other option. Pressing the razor into the machined groove should be avoided for ductile materials because of the risk of inducing residual stresses at the crack tip that might promote higher K_{IC} and G_{IC} values.

In the load vs loading point displacement curve shown in Figure 2.1 (b). AB' is a sketched line with 5% less slope than the AB line, and the corresponding pint to the intersection between the line AB' and the load-displacement curve is P_Q. If P_{max} is between AB and AB', it would be called P_Q, and will be used to calculate K_{Q}. If not, P_Q will be used.

Moreover, if P_{max}/P_Q is less than 1.1, then P_Q is valued to be used; otherwise, the test would be invalid. K_{Q}, which is so far a conditional fracture toughness until pass the validity Eq.2.2, can be calculated using Eq.2.1. Where B and W are the thickness and the width, respectively, and $f(x)$ is a dimensionless factor that depends on the ratio $x = a/W$. K_{Q} becomes K_{IC} when it passes the verification chick of size criteria in Eq.2.2 where K_{Q} is the conditional K_{IC}, and σ_y is the yield stress of the polymer. This relationship will ensure that thickness B is enough to consider the problem following the plane strain condition. The term $(W - a)$ is to ensure preventing plasticity in the ligament while the other side of the equation is representing the small size of the process zone, that the initial assumption of LEFM is based on.

$$K_{\mathrm{Q}} = \left(\frac{P_Q}{BW^{\frac{1}{2}}}\right) f(x) \tag{2.1}$$

$$f(x) = \frac{(2+x)(0.886 + 4.64x - 13.32x^2 + 14.72x^2 - 5.6x^4)}{(1-x)^{\frac{3}{2}}}$$

$$B, a, (W-a) > 2.5\left(\frac{K_Q}{\sigma_y}\right)^2 \tag{2.2}$$

For calculating an accurate critical strain energy release rate G_{IC}, a correction to the load-displacement curve is required duo to pin penetration. That involves loading an unnotched CT sample to the point that the regular specimen would fail then subtracts the resulting area under the curve from the ones obtained from the notched samples. The corrected new energy is representing the required energy for the fracture after subtracting the pin penetration effect. Eq.2.3 is used to calculate G_{IC}, where U is the corrected critical energy or the area under the load-displacement curve, and $\emptyset$ is a dimensionless factor that depends

on the ratio $x = a/W$.

$$G_{\mathrm{IC}} = \frac{U}{(BW\emptyset)} \tag{2.3}$$

$$\emptyset = \frac{(1.9118+19.118x-2.5122x^2-23.226x^3+20.54x^4)(1-x)}{(1.9118-5.0244x-69.678x^2+82.16x^3)(1-x)+2(1.9118+19.118x-2.5122x^2-23.226x^3+20.54x^4)}$$

2.2 Materials and Methods

Two thermoset epoxy resins have been characterized for fracture toughness in this thesis: SC-15 and EPON 862. SC-15, a low-viscosity, rubber toughened epoxy cured with a Cycloaliphatic amine, was obtained from Applied Poleramic (Benicia, CA). EPON 862 (di-glycidyl ether of bisphenol-F epoxy (DGEBF)) and its curing agent 'W' (DETDA (diethyl toluene diamine)) were obtained from Miller-Stephenson Chemical Co. The nanoparticles that were used in this study are Graphene nanoplatelets and nano-silica. Graphene Nanoplatelets (xGnP) are unique nanoparticles consisting of short stacks of graphene. xGnP grade C particles obtained from XG Sciences, consist of aggregates of sub-micron platelets that have a particle diameter of less than 2 microns and a typical particle thickness of a few nanometers with average surface areas of 750 m^2/g [28]. The nano-silica particles (MEK-AC-5140) with an average diameter of 80 nm were obtained from Nissan Chemical American Corporation. Dr. Shiwang Cheng, a faculty member of the Chemical engineering and materials science department of MSU, supplied the particles and prepared the epoxies with the nanoadditive. xGnP were dispersed into EPON 862 and SC-15 in 0.1wt% and 0.5wt% while the nano-silica particles were dispersed only in EPON 862 in 0.1wt% and 0.5wt%. The dispersion method is an essential step for getting the most mechanical bonding and enhancing the mechanical performance. Different dispersion methods were reviewed in section 1.3.2.

xGnP were directly dispersed in Tetrahydrofuran (THF) at a concentration of 0.1wt%. The Graphene/THF suspension was further dispersed with 1-hour sonication before dispersing into EPON 862 and SC-15. The Nano-silica particles (MEK-AC-5140) were first precipitated into Hexane and resuspended into Tetrahydrofuran (THF) up to a concentration of 10wt% before dispersing into the EPON 862. After the epoxies being delivered by Dr.Cheng, we still have one more step to prepare them for manufacturing, which is solvent evaporation.

For epoxies prepared with the nanoparticles, full evaporation of the solvent is needed before starting to mix the epoxies with the curing agents. Otherwise, a massive reduction in the mechanical properties will occur. There are multiple methods to evaporate solvents, depending on the amount of solvent and equipment availability. In our situation, a vacuum chamber was used to reduce the boiling temperature of the solvent; however, it was found to be inadequate. Subsequently, a heating source was used to reduce viscosity and to make it easier for the solvent to be released, Figure 2.2. For the last stage of the evaporation, stirring the epoxies were needed to ensure the removal of all unwanted solvent. All these steps were weight monitored by weighting the mixture to confirm getting rid of all the solvent. These steps took an average of six days.

2.2.1 Curing Cycle and Specimen Preparation

The mixing weight ratio of the epoxies to curing agents is 100:30 for SC-15 and 100:26.4 for EPON 862, as recommended by the manufacturer. The mixture of the two systems was degassed using a regular vacuum chamber to remove the bubbles created during the stirring process. It took 25 min to remove all bubbles in SC-15. For EPON 862, additional heating is required since EPON 862 has a higher viscosity compared to SC-15. After degassing, the resins were poured into the preheated silicon molds. The silicon molds were made with a

Figure 2.2: Solvent evaporation process.

stainless steel prototype, which was machined using Electrical Discharging Machine (EDM), as shown in Figure 2.3.

After pouring the mixture, the silicon molds were placed into an oven and subjected to a cure cycle flowing literature [18, 29] and considering manufacturer recommendations. For SC-15, the samples were cured at 60 °C for 4 hours and then post-cured at 121 °C for other 3 hours. For EPON 862, the cycle has two ramps: the first one for 30 min from 90 °C to 121 °C, then maintaining at 121 °C for 2h. The second ramp is for another 30 min from 121 °C to 177 °C and then maintains the temp at 177 °C for another 2 h. After the curing cycle finished, the molds were cooled to room temperature, and the samples were ready to be tested, see Figure 2.4.

As shown in Figures 2.5 and 2.6, the original color of EPON 862 samples is yellow

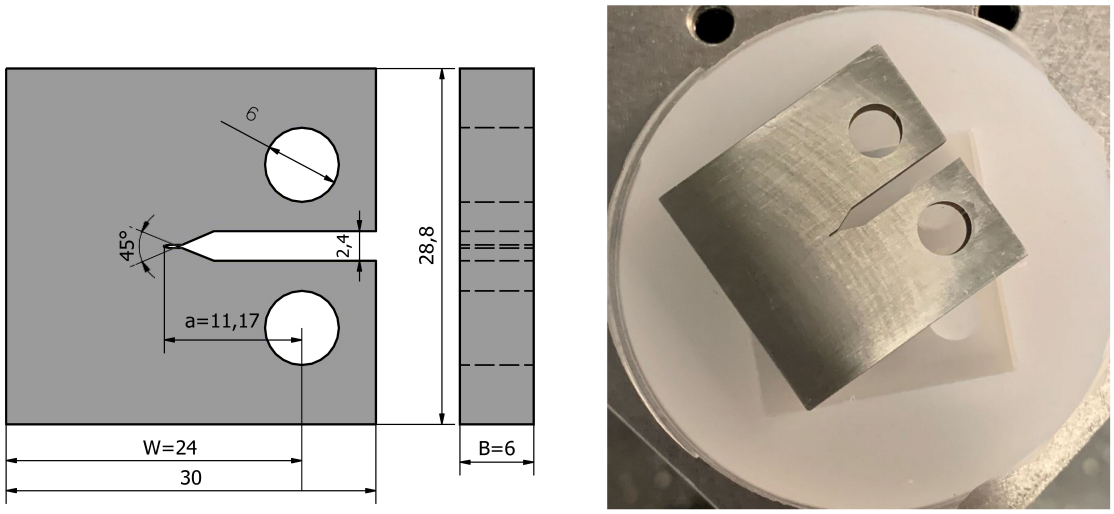

(a) (b)

Figure 2.3: Sample's design and silicon molds: (a) The design the stainless steel prototype in (mm) following the standards [5]. (b) The stainless steel prototype and the silicon mold.

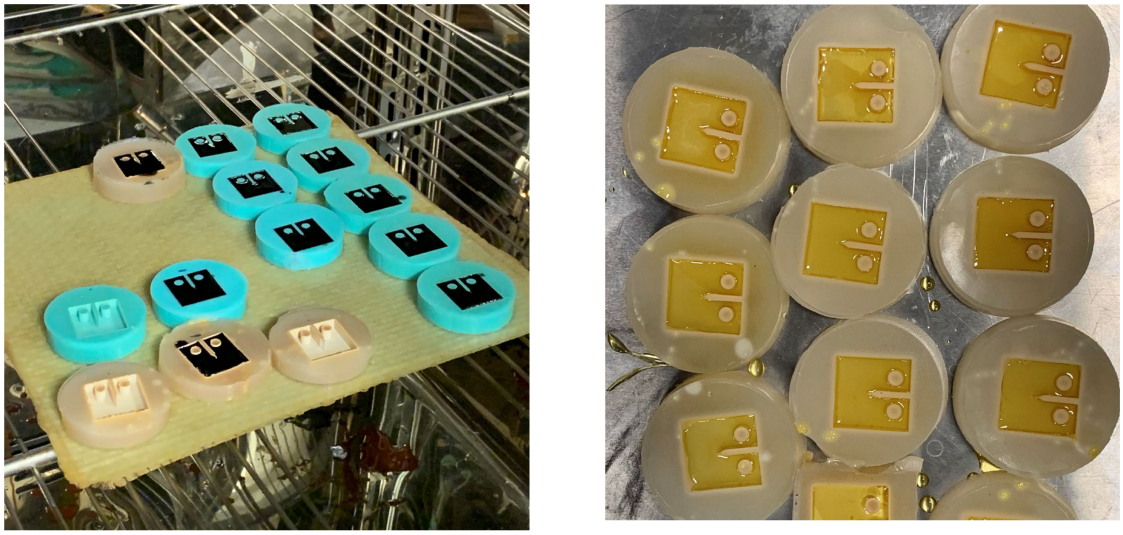

(a) (b)

Figure 2.4: After completing the curing cycle: (a) Samples lift inside the open door oven to cool down after finishing the curing cycle. (b) Samples are ready to be carefully extracted from the molds.

and transparent, whereas SC-15 samples are white and opaque. After adding 0.1wt% of xGnP, the EPON 862 samples turned in black while the SC-15 samples became dark gray. With 0.5wt% of xGnP, EPON 862 stayed black and the SC-15 changed to fully black. For EPON 862 samples with 0.1wt% and 0.5wt% of nano-silica, the samples lost its transparent gradually. For digital image correlation (DIC) measurement, all samples have been painted with white and then black spray paint to create speckles on surface.

Figure 2.5: SC-15 samples, from right: baseline, 0.1wt%, then 0.5wt% of xGnP.

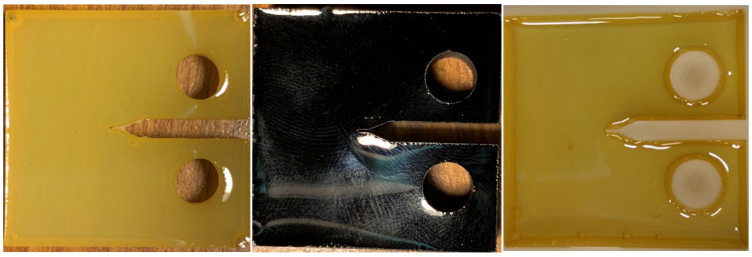

(a) (b) (c)

Figure 2.6: EPON 862 samples: (a) 0.1wt%,0.5wt% of nano-silica. (b) 0.1wt%,0.5wt% of xGnP. (c) Baseline.

2.3 Experiment Setup

For the fracture toughness Mode I experiment, ASTM standard D5045 [5] has been followed. The experiments were performed using the MTS Insight Electromechanical test frame with 10 KN loading unit, as shown in Figure 2.7. To capture the images during experiment for DIC measurement, a Stingray camera with image pre-processing by Allied Vision was used.

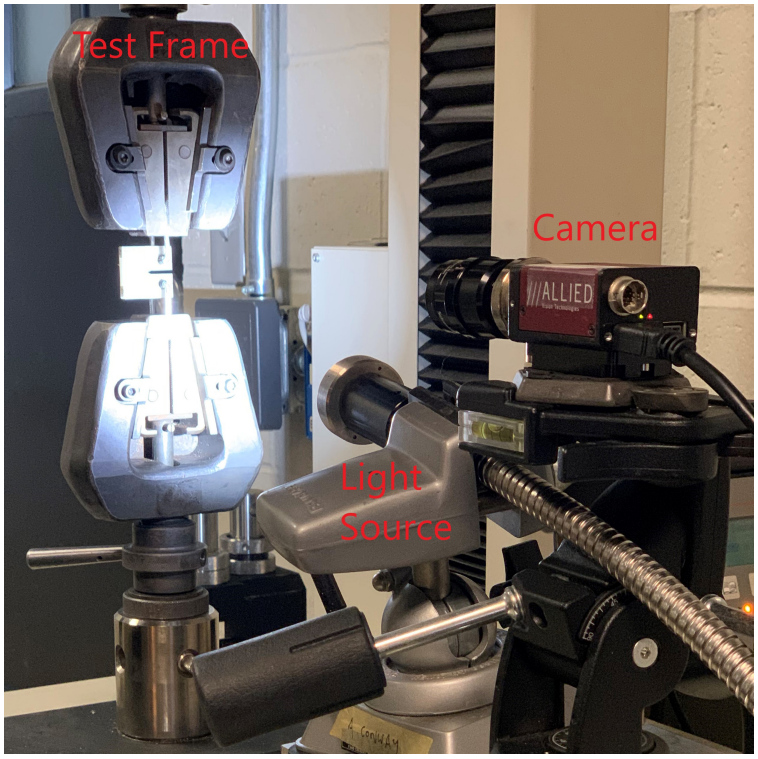

Figure 2.7: The experiment setup with camera and light source.

The images were recorded at a rate of 20 images per second to match the machine's sampling rate of 20 Hz. The tests running time were about 3 to 5.5 seconds depending on the material and the amount of deflection needed for fracture with cross-head speed 10 mm/min. Duo to the small size of the CT specimen used in this work, instead of using standard compact tension (CT) fixture, an alternative loading method was developed as shown in Figure 2.8. A 5mm hollow tension pin and a tough copper aluminum wire were used to link the specimens to the testing machine using the regular tensile grip. Additional attention was paid to the samples' alignment for every trial to ensure having the load perpendicular to the crack surface. The dimensions, the initial and final crack length of the samples were measured per ASTM standard D5045. After performing the test and obtaining data and images, DIC analysis was performed and the result will be discussed in chapter 3.

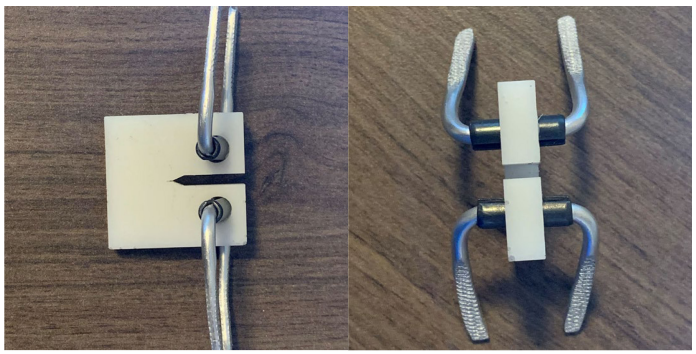

(a) (b)

Figure 2.8: Samples arrangement before attaching to the tensile grip: (a) Front view. (b) Side view.

2.4 Data Acquisition

DIC is a full-field, non-contact optical technique for the measurement of deformation, and strain on the surface of materials and structures. It can be used in both static and dynamic conditions, and its applications range from micro size testing to large structures. In mechanical testing such as tensile, torsion, bending, and fracture testing, DIC has been used to replace strain gauge and extensometer measurement.

DIC analysis was performed using GOM software. The four images in Figure 2.9 show the typical deformation process of a CT specimen in fracture testing. Using an optical extensometer defined in GOM, the displacement at the loading point was measured. The load-displacement curve was then used to calculate the energy release rates. This method is more accurate than the displacement recorded by the cross-head displacement of the testing machine. Another measurement was the Crack tip opening displacement (CTOP). CTOP is a fracture criterion associated with EPFM. It is also helpful for recording the small plasticity at the crack tip. The positions where the loading-point displacement and CTOD were measured were indicted in Figure 2.9. The DIC displacement resolution is $\sim \pm 0.002mm$, and the DIC strain resolution is $\sim \pm 0.1\%$.

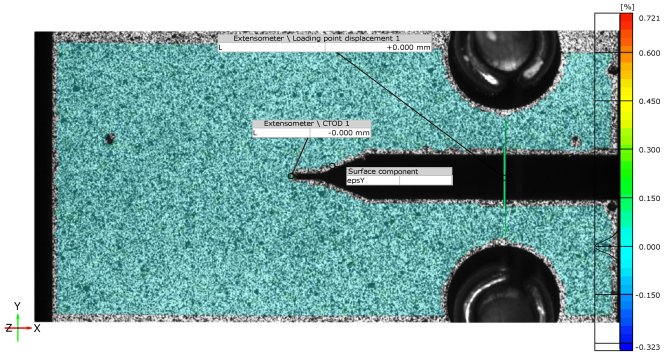

(a)

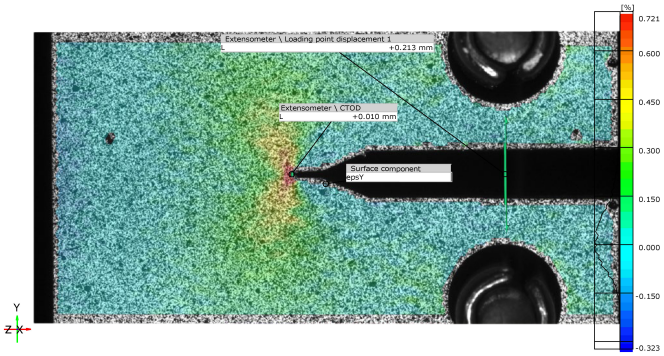

(b)

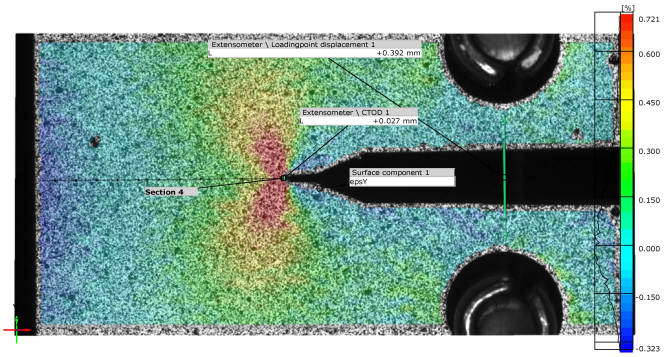

(c)

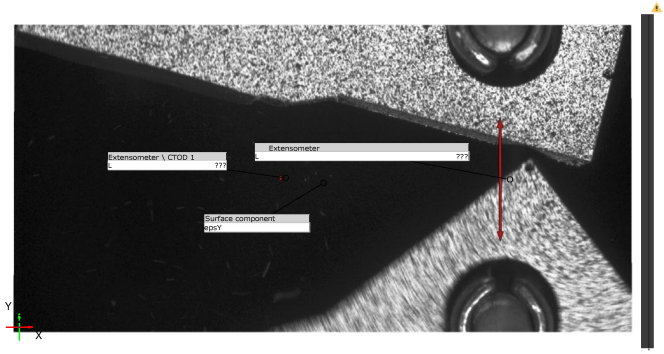

(d)

Figure 2.9: The experiment's stages until the fracture: (a) The second still image. (b) The middle of the test. (c) The moment before the fracture. (d) The moment after the fracture.

Chapter 3: Results and Dissection

In this chapter, the effect of pre-cracking method was examined using the results of EBON 862 specimens. Then the experimental results of fracture toughness of two epoxies with the nano-additives are presented. In the last section, the crack tip plastic zones were analyzed, and the results were compared with the experimental observations.

3.1 Different Pre-cracking Procedures and their Effects

The purpose of pre-cracking is to introduce an initial crack similar to that naturally produced during crack propagation process. The measured fracture toughness depends on the way how the initial crack is introduced. To investigate the influence of initial crack, McAninch [29] created the crack by several methods, such as inserting different types of thin films into polymer samples before curing; scoring the samples with a thin double- edged razor blade; and using thick single-edged razor to make "instantly propagated" cracks, i.e. a natural crack propagated after the razor tip. It was found that, unlike instantly propagated cracks, the specimens with initial crack by razor scoring or inserting thin films yielded higher fracture toughness values. McAninch's study raises the significance of having a sharp crack in fracture toughness measurement.

ASTM D5045 standard recommends a pre-cracking procedure using a razor. To create a pre-crack in a notched specimen, it suggests that one can either tape the razor by hand or apply a sliding motion. In this work, both methods have been tried. However, taping by hand was not sufficient to introduce an initial crack. To increase the load, a mechanical vise was employed to press the blade into the notch, as shown in Figure 3.1(a). On the other

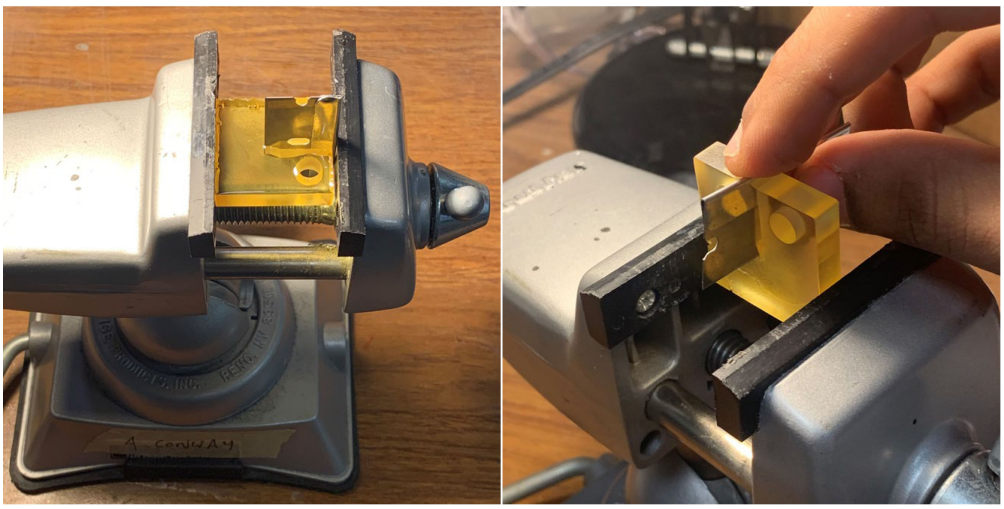

(a) (b)

Figure 3.1: The two methods of pre-cracking: (a) Pressing the razor into the notch. (b) Sliding the razor on the notch.

hand, the method of applying a sliding motion was successful to generate an initial crack. This method is shown in Figure 3.1(b).

Table 3.1 presents the fracture toughness values measured with three EPON 862 baseline specimens: one with the initial crack generated by pressing the razor into the notch, and the other two with the initial crack generated by sliding motion. The K_{IC} value of the specimen pre-cracked by forcing the razor into the sample is $\approx 1.99\ MPa.\sqrt{m}$, and for G_{IC} is $\approx 1397\ J/m^2$. The two specimens pre-cracked by sliding the razor yielded lower fracture toughness. The measured values were $\approx 1.25\ MPa.\sqrt{m}$ and $\approx 0.75\ MPa.\sqrt{m}$ in K_{IC}, and $\approx 623\ J/m^2$ and $\approx 201\ J/m^2$ in G_{IC}. The results show that pre-crack made by pressing the razor led to a much higher measured fracture toughness than that made by sliding motion. Furthermore, EPON 862 baseline material appeared to be very sensitive to the pre-cracking process. Even for the specimens pre-cracked with the same sliding motion, the measured fracture toughness was quite different.

Table 3.1: Comparison between two different pre-cracking methods on EPON 862's fracture toughness

	$K_{\mathbf{IC}}$ $(MPa.\sqrt{m})$	$G_{\mathbf{IC}}$ (J/m^2)
Sliding	0.75	201
Sliding	1.25	623
Pressing	1.99	1397

Table 3.2 compares the fracture toughness values measured with two SC-15 baseline specimens. Again, the pre-crack introduced by pressing the razor yielded a higher fracture toughness value than the one with sliding motion. It was suspected that pre-cracking by pressing the razor may introduce local compressive residual stresses at the crack-tip. To examine this effect, DIC was used to measure the strain field before and after the pre-cracking procedure by pressing the razor. Figure 3.2 presents the DIC results for a EPON 862 baseline specimen in this process. As shown, pre-cracking left a compressive residual strain field at the crack tip. The measured maximum ϵ_x strain value was -6.672 %. With a compressive residual stress normal to the crack surface, the force required for Mode-I type crack propagation would be higher. This example shows that the measured higher fracture toughness using specimens pre-cracked by pressing the razor is the artifact of improper pre-cracking method. It is noted that the fracture toughness measurement for SC-15 appeared to be less sensitive to the pre-cracking method as compared that to EPON 862. This can be attributed to the fact that SC-15 neat resin is rubber toughened. It is not as brittle as EPON 862 neat resin. Indeed, the xGnP and the Nano-silica modified EPON 862 resins were less sensitive to pre-cracking process, as to be discussed in the next section.

Table 3.2: Comparison between two different pre-cracking methods on SC-15's fracture toughness

	$K_{\mathbf{IC}}$ $(MPa.\sqrt{m})$	$G_{\mathbf{IC}}$ (J/m^2)
Sliding	1.547	965
Pressing	2.12	1550

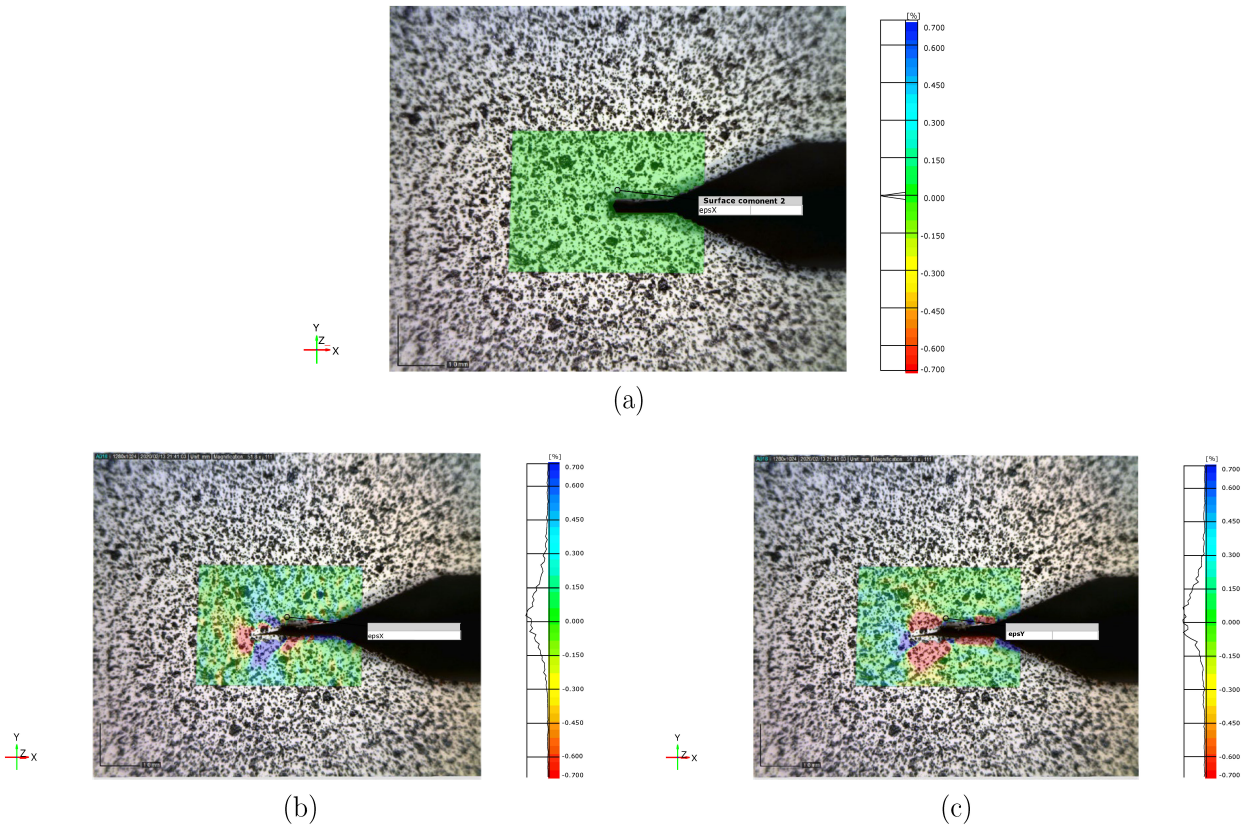

Figure 3.2: The strain field of the pressed sample: (a) Before inserting the blade. (b) ϵ_x after inserting the blade. (c) ϵ_y after inserting the blade.

3.2 Fracture toughness Results

The Mode-I fracture toughness of the EPON 862 and SC-15 baseline resins and the nano additive modified two resins was measured following ASTM D5045 standard using CT specimens pre-cracked by using a razor with sliding motion. The critical stress intensity factor K_{IC} and the critical energy release rates G_{IC} were determined.

3.2.1 EPON 862

Figure 3.3 compares the typical load-displacement curves of EPON 862 baseline and EPON 862 with 0.1 and 0.5 weight fractions (wt%) of xGnP. As can be seen, adding xGnP increased the slop of the load-displacement curves and the maximum load. However, it did not change the shape of the curve. All samples exhibited a linear curve up to failure, indicating brittle fracture. Therefore, the maximum loads were used to calculate the fracture toughness value.

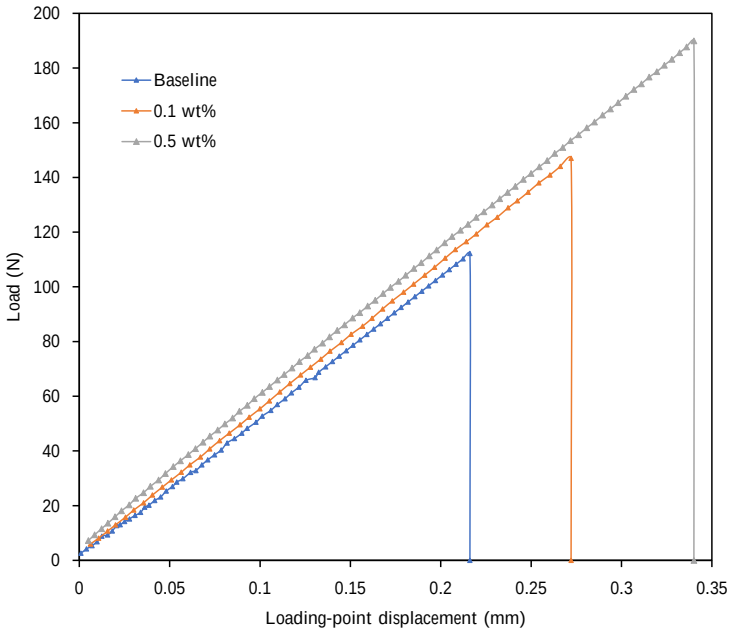

Figure 3.3: Load vs Loading-point displacement of EPON 862 with xGnP.

Figure 3.4 and Tables 3.3, 3.4 compare the fracture toughness values of EPON 862 resins. The baseline samples were sensitive to the pre-cracking and therefore the scatter in measured fracture toughness values was high. This is shown by the relatively high standard deviation (SD) and the standard error of the mean (SEM) values. xGnP modified EPON 862 showed much smaller scatter in fracture toughness measurement. Adding 0.1wt% of xGnP resulted an improvement in K_{IC} by $\sim 44.87\%$ and G_{IC} by $\sim 87.38\%$. Adding 0.5wt% of xGnP further improved K_{IC} by $\sim 70\%$, and G_{IC} by $\sim 156.6\%$.

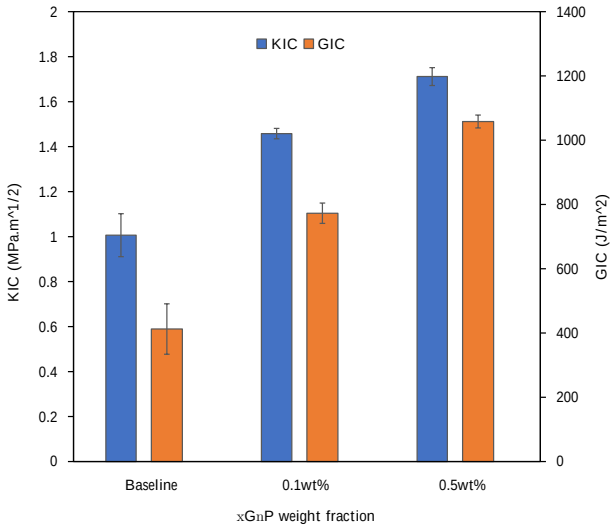

Figure 3.4: K_{IC} and G_{IC} of EPON 862 with xGnP.

Table 3.3: K_{IC} $(MPa.\sqrt{m})$ averages of EPON 862 with xGnP

	$K_{\mathbf{IC}}$	SD	SEM	Improvement	No. S
Baseline	1.0063	±0.27	±0.095	-	8
0.1wt%	1.4578	±0.05	±0.023	44.87%	5
0.5wt%	1.7114	±0.09	±0.039	70%	5

Table 3.4: G_{IC} (J/m^2) averages of EPON 862 with xGnP

	$G_{\mathbf{IC}}$	SD	SEM	Improvement	No. S
Baseline	412	±221	±78	-	8
0.1wt%	772	±70	±31	87.38%	5
0.5wt%	1058	±44	±20	156.59%	5

To examine the reinforcing effect of different nano fillers, EPON 862 has also been modified with nano-silica. The results are show in Figure 3.5 and Tables 3.5, 3.6. Adding 0.1wt% nano-silica, the improvement to K_{IC} was $\sim$ 30.76% and $G_{\mathrm{IC}} \sim$ 48.85%. With 0.5wt% of nano-silica, K_{IC} was increased by $\sim$ 43.697%, and G_{IC} by $\sim$ 86.52%. Comparing with the results of xGnP, the improvement with nano-silica was about a half of the value of that with xGnP, as shown by Figure 3.5. The results show that xGnP is a more sufficient additive to EPON 862 than nano-silica.

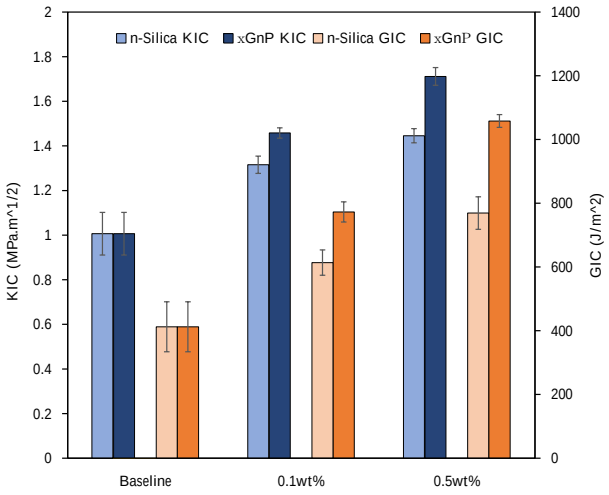

Figure 3.5: Comparison between EPON 862 with xGnP and EPON 862 with Nano-Silica for different weight fractions.

Table 3.5: K_{IC} $(MPa.\sqrt{m})$ averages of EPON 862 with Nano-silica

	K_{IC}	SD	SEM	Improvement	No. S
Baseline	1.0063	±0.27	±0.095	-	8
0.1wt%	1.3154	±0.07	±0.038	30.76%	4
0.5wt%	1.4456	±0.06	±0.031	34.69%	4

Table 3.6: G_{IC} (J/m^2) averages of EPON 862 with Nano-silica

	G_{IC}	SD	SEM	Improvement	No. S
Baseline	412	±221	±78	-	8
0.1wt%	613	±79	±39	48.58%	4
0.5wt%	769	±102	±51	86.52%	4

3.2.2 SC-15

For SC-15, the results showed a slight improvement in both the stress intensity factor K_{IC} and strain energy release rate G_{IC} when adding 0.1wt% of xGnP. However, the enhancement started to diminish for having 0.5wt% of the same particles.

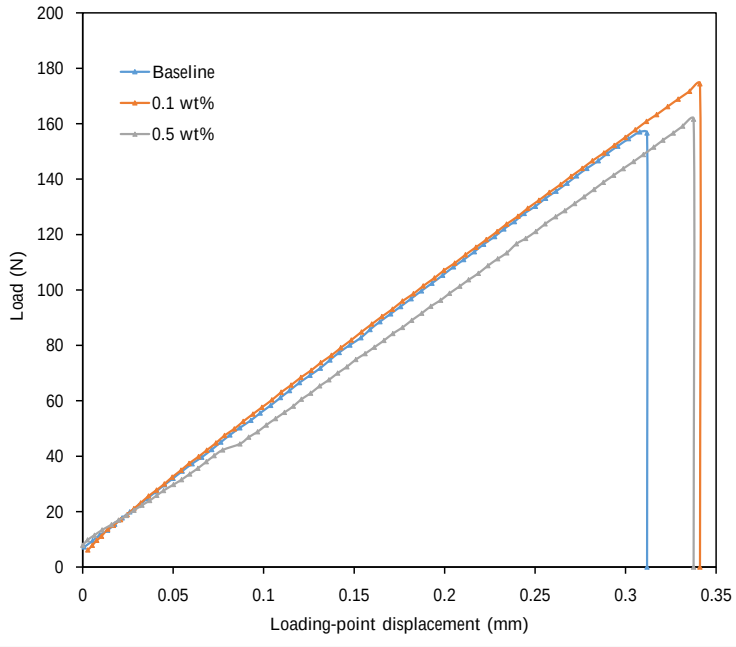

Figure 3.6: Load vs Loading-point displacement of SC-15 with xGnP.

Figure 3.6 compares the typical load-displacement curves of SC-15 baseline resin and SC-15 modified with xGnP. All three types of samples displayed a brittle fracture. SC-15 with 0.1wt% showed a slightly higher maximum load. However, the curve for SC-15 with 0.5wt% xGnP displayed a slope even lower than the baseline, indicating a lower stiffness of this specimen. A CT specimen can have lower stiffness as each specimen may have a unique initial crack length. To preclude this effect, the initial crack lengths of all CT specimens were examined to ensure that the load-displacement curves of three types of SC-15 samples were compared using the specimens with similar initial crack length. It was found that the slopes for the load-displacement curves of SC-15 with 0.5wt% xGnP were consistently lower

than the two other types of SC-15 samples. This could be caused by residual solvent in this type of samples. When solvent is not removed completely, the nano additive modified epoxy resin can behave softer than the baseline resin. Therefore, the data with SC-15 with 0.5wt% xGnP presented here should be treated with caution.

Figure 3.7 and Tables 3.7, 3.8 compare the fracture toughness of SC-15 baseline resin and SC-15 with 0.1Wt%, 0.5wt% xGnP . Unlike the case of brittle EPON 862 baseline sample, SC-15 baseline samples were not sensitive to the pre-cracking. Adding 0.1wt% of xGnP result in an improvement of K_{IC} by $\sim$ 8.81% and G_{IC} by $\sim$ 21%. SC-15 with 0.5wt% of xGnP resulted much smaller improvement in fracture toughness. K_{IC} improved by $\sim$ 2.63% and the G_{IC} increased by $\sim$ 14.6%. This limited enhancement in the fracture toughness may be attributed to the fact that SC-15 is already rubber toughened. On the other hand, the result for SC-15 with 0.5wt% of xGnP presented here may not reflect the real trend. As stated previously, it is possible that the solvent was not removed completely in this type of material.

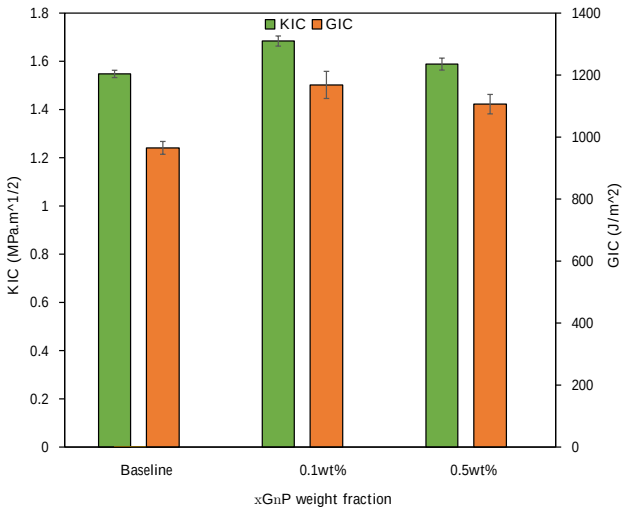

Figure 3.7: K_{IC} and G_{IC} of SC-15 with xGnP.

Table 3.7: K_{IC} $(MPa.\sqrt{m})$ averages of SC-15 with xGnP

	$K_{\mathbf{IC}}$	**SD**	**SEM**	**Improvement**	**No. S**
Baseline	1.5476	±0.03	±0.015	-	5
0.1wt%	1.6840	±0.05	±0.020	8.81%	7
0.5wt%	1.5884	±0.06	±0.024	2.63%	7

Table 3.8: G_{IC} (J/m^2) averages of SC-15 with xGnP

	$G_{\mathbf{IC}}$	**SD**	**SEM**	**Improvement**	**No. S**
Baseline	965	±46	±20	-	5
0.1wt%	1168	±115	±43	21%	7
0.5wt%	1106	±83	±31	14.6%	7

3.3 Stress Distribution and Plasticity Correction

The crack tip stress field is a classic problem of fracture mechanics. For a center crack in an infinitely large plate subjected to biaxial loading, the LEFM solution for elastic stresses near the crack-tip has been provided by Westergaard [24]. For Mode-I loading

$$\begin{aligned} \sigma_x &= \frac{K}{\sqrt{2\pi r}}\left[\cos\frac{\theta}{2}\left(1-\sin\frac{\theta}{2}\sin\frac{3\theta}{2}\right)\right] \\ \sigma_y &= \frac{K}{\sqrt{2\pi r}}\left[\cos\frac{\theta}{2}\left(1+\sin\frac{\theta}{2}\sin\frac{3\theta}{2}\right)\right] \\ \tau_{xy} &= \frac{K}{\sqrt{2\pi r}}\left(\sin\frac{\theta}{2}\cos\frac{\theta}{2}\cos\frac{3\theta}{2}\right) \end{aligned} \tag{3.1}$$

Where K is the Mode-I stress intensity factor, r is the distance to the crack tip, θ is the angle to the x-axis measured at the crack tip, as shown in Figure 3.8.

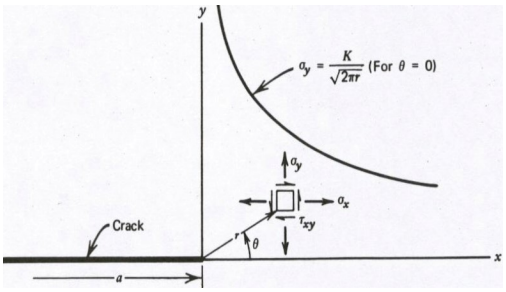

Figure 3.8: The stress field near the crack tip.

A limitation of LEFM is the stress singularity at the crack-tip. In Eq 3.1, when r approaches to zero, the σ_x and σ_y stress components become infinite. In reality, a plasticity region will develop near the crack tip whenever the stress exceeds the yield strength of the material as the crack tip radius must be finite [6,30,31]. Simple correction to LEFM, such as the Irwin approach are available when moderate crack tip yielding occurs [6], For substantial yielding, other parameters such J-integral for the nonlinear material behavior must be taken into account.The crack-tip plastic size can be estimated by two methods: the Irwin approach and the strip yield model [6]. The Irwin approach uses the elastic stress analysis to estimate the elastic-plastic boundary. Note that the term plastic zone usually referred to metals, but it is used here to describe the inelastic crack tip behavior [6]. The estimation of the plastic zone length begins by calculating the normal elastic stress σ_y directly ahead of the crack along $\theta = 0$. As the first approximation, the boundary between elastic and plastic zone occurs when the elastic stresses satisfy a yield criterion in Eq. 3.2.

$$\sigma_y = \frac{K}{\sqrt{2\pi r_y}} = \sigma_{ys} \tag{3.2}$$

For plane stress conditions, yielding occurs when $\sigma_y = \sigma_{ys}$. Solving for r_y gives a first-order estimate of plastic zone size as expressed in Eq 3.3.

$$r_y \approx \frac{1}{2\pi}\frac{K^2}{\sigma_{ys}^2} \quad \text{(plane stress)} \tag{3.3a}$$

$$r_y \approx \frac{1}{6\pi}\frac{K^2}{\sigma_{ys}^2} \quad \text{(plane strain)} \tag{3.3b}$$

This process is illustrated in Figure 3.9. When yielding occurs, stresses must be redistributed to satisfy the equilibrium. For plane strain conditions, yielding is suppressed by the

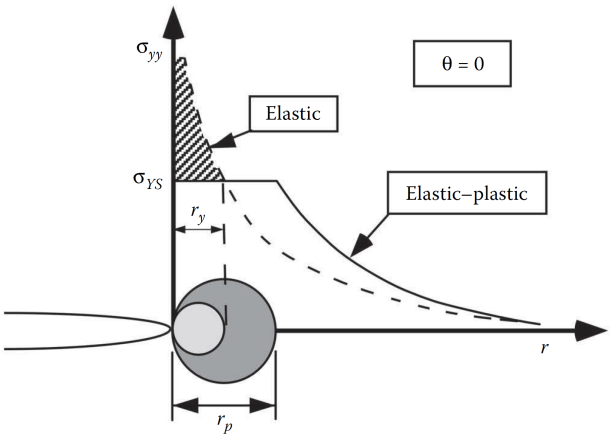

Figure 3.9: First-order and second-order estimates of plastic zone size (r_y and r_p, respectively). The cross-hatched area represents the load that must be redistributed, resulting in a larger plastic zone. Obtained from [6].

triaxial stress state, and the Irwin plastic zone correction is reduced by a factor of 3 as in Eq 3.3b [6]. However, specimens always follow plane stress conditions at the surface since there is no σ_z constrain the deformation in the through-thickness direction.

Following Irwin's approach, σ_y stress distribution along the crack surface for several CT specimens has been calculated. First, the elastic stress was calculated using Eq.3.1. Next, the first order plastic zone size was estimated using Eq.3.3a. The σ_y stress distribution was then shifted to the appropriate position. As discussed earlier, DIC was used in fracture testing to monitor the displacement and strain fields. Using DIC results, the stress distributions near the crack-tip can be verified. In this work, the stress field just before final fracture was examined.

From the DIC images captured just before the final fracture, the three strain components in the front of the crack path were determined. σ_y stress along the same path was determined using 3D Hooke's law. If the von-Mise stress value at a point exceeds the yield strength, it is assumed to fall into the plastic zone and subsequently the stress value is reduced to the value of the yield strength. The mechanical properties of the SC-15 is listed in Table 3.9.

Table 3.9: Mechanical Property of SC-15 baseline.

Young's modulus (E)	Yield Strength (σ_{ys})	Poisson's ratio (v)
2.5 GPa	60 MPa	0.33

The von-Mises stress is calculated by Eq.3.4 where σ_1,σ_2, and σ_3 are the principal stresses and σ_v is the von-Mises stress. The assumption is that the material start yielding when the von-Mises stress reaches the yield strength σ_{ys}.

$$\sigma_v = \frac{1}{\sqrt{2}} \left[(\sigma_1 - \sigma_2)^2 + (\sigma_1 - \sigma_3)^2 + (\sigma_2 - \sigma_3)^2 \right]^{\frac{1}{2}} \tag{3.4}$$

Three SC-15 specimens with 0.5wt% xGnP were examined as listed in Table 3.10. The procedure to calculate the experimental σ_y stress distribution and the experimental plastic zone is illustrated using specimen 1. From DIC, the strain components were recorded for each point near the crack-tip along the crack path with $\theta = 0$. For example, the strain components of the first point are ϵ_x=-0.4259%,ϵ_y=3.008%, ϵ_z=-2.482%, and $\epsilon_{xy} \approx 0\%$. The corresponding stresses were calculated using 3D Hooke's law and the stress components were found to be σ_x= -9.86 MPa, σ_y= 56.42 MPa. Then, the von-Mises stress σ_v in Eq.3.4 was calculated from the principal stresses of the stress components, and it's found to be σ_v=61.9 MPa. That means this point fall into the plastic zone. For the second point, the corresponding stresses were σ_x= -11.09 MPa, σ_y= 53.64 MPa. The von Mises stress is σ_v = 60 MPa = σ_{ys}. This point was set as the elasticity limit since the effective stress reaches the yield strength and the previous point were reduced to this limit, as shown in Figure 3.10. From this limit, the corresponding length from the crack tip was set as the estimated experimental plastic zone, and it is found to be 24 μm for this sample.

This process was repeated for all DIC points near the crack using Excel, and the curves of σ_y were plotted. For the second and the third specimen, the same process was preformed.

Table 3.10: The three example samples of SC-15 with 0.5wt% xGnP.

	Specimen 1	Specimen 2	Specimen 3
Pre-cracking method	Sliding	Sliding	One round sliding
Width W (mm)	24.2	23.92	23.8
Crack length a (mm)	11.48	11.13	11.06
Thickness B (mm)	6.04	5.9	6.12
Critical displacement (mm)	0.33	0.39	0.48
P_Q (N)	161	159	228
K_{IC} ($MPa.\sqrt{m}$)	1.538	1.545	2.1
G_{IC} (J/m^2)	946	1101	1835
First-order plastic zone r_y (μm)	104	105	195
Second-order plastic zone r_p (μm)	208	210	390
Experimental plastic zone (μm)	24	196	311

The estimation of the experimental plastic zone was found to be 196 μm and 311 μm for the second and third specimen respectively.

Figure 3.10 for the first sample and Figure 3.11 for second sample shows the theoretical and the experimental stress for the normal y-direction. Based on each sample parameters, the elastic stress distribution was drawn using Eq.3.1 for both samples. Using Eq.3.3b, the first-order plastic zone r_y was found to be 34.87 μm for the first sample and 35.20 μm for the second one while the second-order of plastic zones are double the first. Based on that, a new line has been placed for the redistributed stress, considering the plastic zone.

The first two samples have a fracture load about 160 N and their K_{IC} values were very close. However, the critical loading point displacement (u) and critical strain energy release rate (G_{IC}) values were different. The first sample has a critical displacement of 0.33 mm and G_{IC} of 946 J/m^2 while the second one has a critical displacement of 0.39 mm and G_{IC} 1101 J/m^2.The first sample fractured as it reached the yield strength of the material with a plastic zone much smaller than the Irwin plastic zone estimation, while the second sample cracked with a plastic zone quite similar to the Irwin plastic zone estimation.

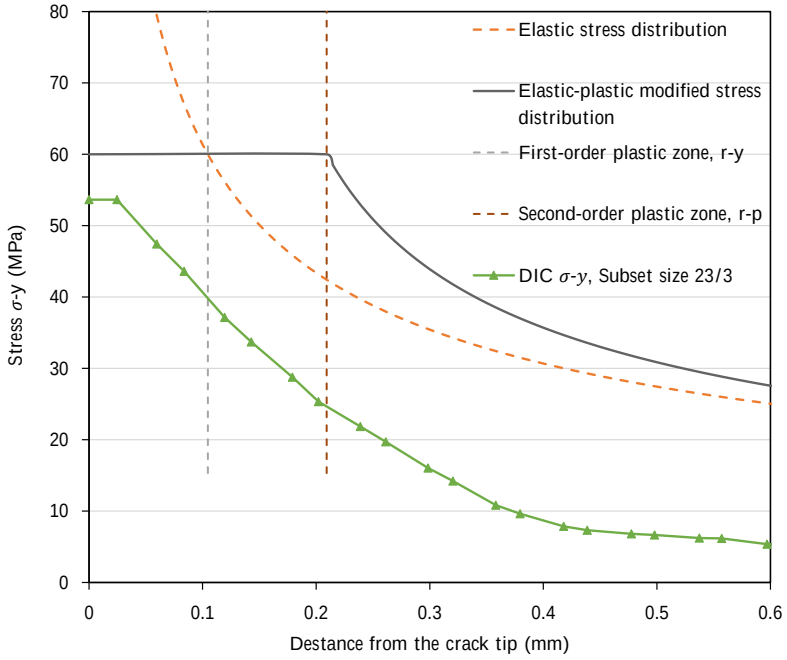

Figure 3.10: The first specimen's normal stress σ_y distribution along the crack path just before the fracture.

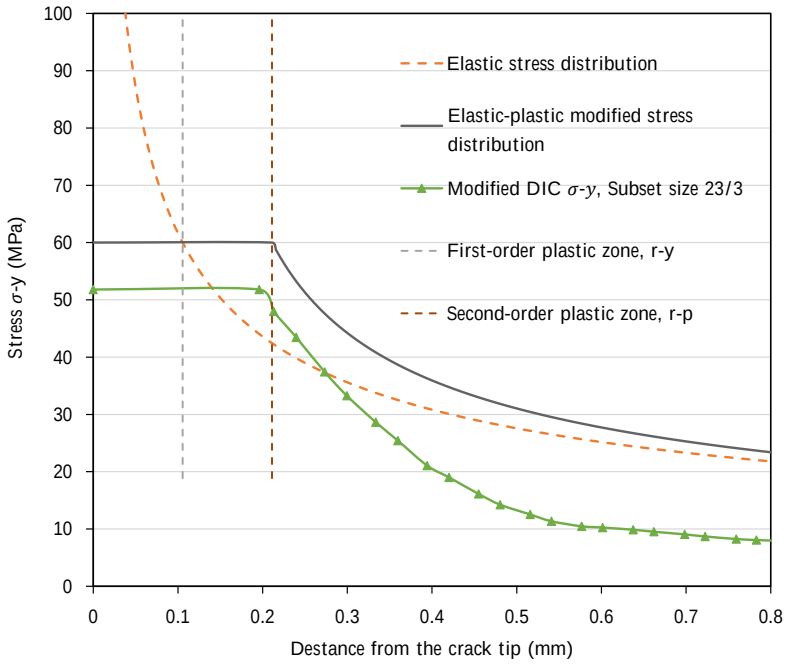

Figure 3.11: The second specimen's normal stress σ_y distribution along the crack path just before the fracture.

The third sample in Table 3.10 and Figure 3.12 that was not correctly pre-cracked recorded a higher critical load about 228 N, higher K_{IC} about 2.1 $MPa.\sqrt{m}$, and a higher G_{IC} about 1835 J/m^2. The theoretical solution of the stress distribution also compared to the experimental stress for the normal y-direction, as it can be seen in Figure 3.12. The sample fractured as it reached the yield strength of the material with a plastic zone less than the Irwin plastic zone estimation by 25%.

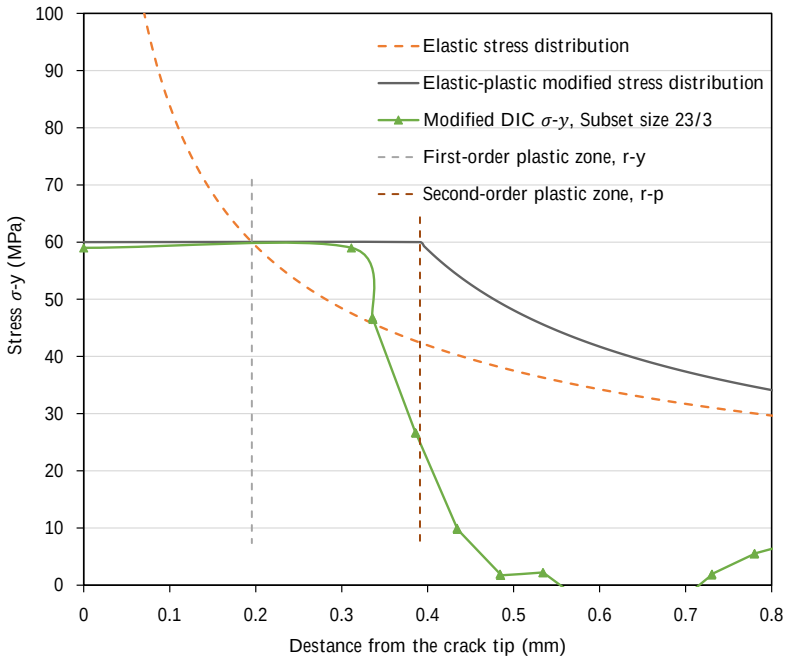

Figure 3.12: The third specimen's normal stress σ_y distribution along the crack path just before the fracture.

The typical (loading-point displacement versa loading)'s curves, that used for determining the energy needed for the fracture, are not giving any induction of plasticity at the crack tip. All curves show liner relationship until the fracture occurs. However, the crack tip opening displacement (CTOD) is found to reflect this if the sample has a plasticity region around the crack tip and how far. For the three samples discussed earlier, an optical extensometer is used to obtain the CTOD and the difference between these samples became clear. As

shown in Figure 3.13, the first sample appeared to have a very small plastic zone while the third sample has the most. This method of analysis differentiated between the first and the second sample in term of plastic zone whereas according to the LEFM theories the values were very close. CTOD is associated with the Elastic-Plastic Fracture Mechanics EPFM; however, it is evident that this measurement is also relevant to the LEFM especially under the plane strain conditions because of the small plastic zone around the crack tip.

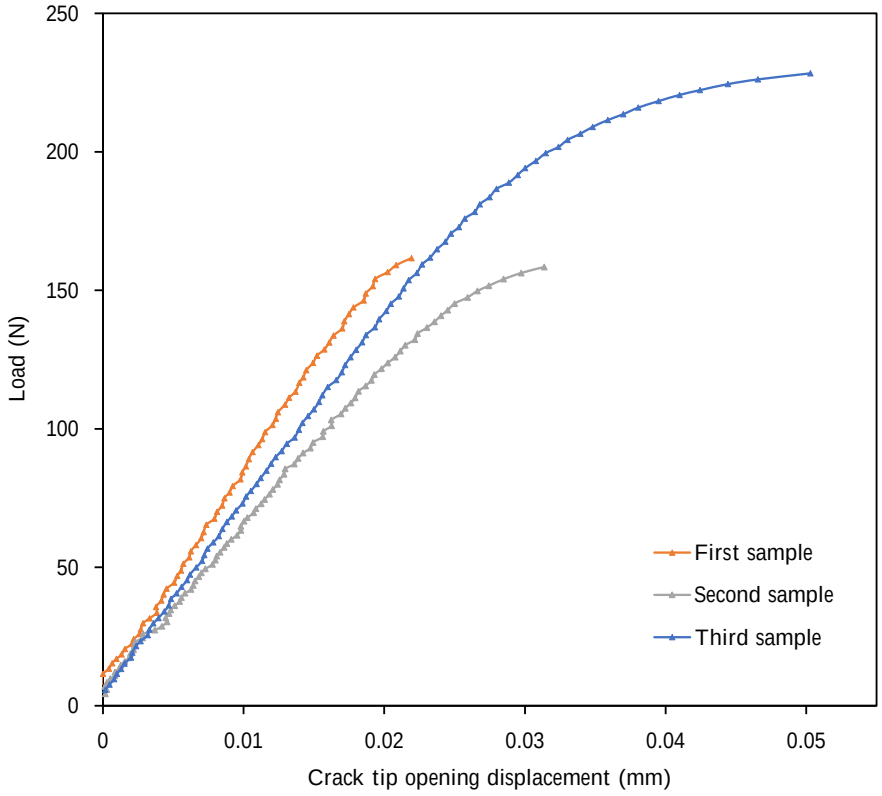

Figure 3.13: Load vs CTOD for the three samples.

3.3.1 Creager and Paris (1967)'s Estimation

The stress field Equations 3.1 and Creager and Paris [32] Equations 3.5 are the two sets of equations describing the elastic stress field near the crack tip. Creager and Paris (1967) Equations 3.5 has the Westergaard part of the solution plus considering the blunting effect. With Creager and Paris's Equations 3.5, we have a finite stress distribution considering the crack tip radius while with Equations 3.1, Irwin modification was needed to limit the infinity. Stress field Equations 3.1 estimates that σ_y equals σ_x for a very sharp crack tip; however, that isn't suitable for a real material. Instead, Creager and Paris (1967) looked at the solution from a different perspective by stating that the crack tip in actual material would be blunt, and the tip would have a radius (ρ). So that the σ_x starts from 0 at the crack tip and then reaches the maximum value at a short distance.

$$\begin{aligned}
\sigma_x &= \frac{K}{\sqrt{2\pi r}}\left[\cos\frac{\theta}{2}\left(1-\sin\frac{\theta}{2}\sin\frac{3\theta}{2}\right)\right]+\frac{K}{\sqrt{2\pi r}}\frac{\rho}{2r}\left(-\cos\frac{3\theta}{2}\right)\\
\sigma_y &= \frac{K}{\sqrt{2\pi r}}\left[\cos\frac{\theta}{2}\left(1+\sin\frac{\theta}{2}\sin\frac{3\theta}{2}\right)\right]+\frac{K}{\sqrt{2\pi r}}\frac{\rho}{2r}\left(\cos\frac{3\theta}{2}\right)\\
\tau_{xy} &= \frac{K}{\sqrt{2\pi r}}\left(\sin\frac{\theta}{2}\cos\frac{\theta}{2}\cos\frac{3\theta}{2}\right)+\frac{K}{\sqrt{2\pi r}}\frac{\rho}{2r}\left(-\sin\frac{3\theta}{2}\right)
\end{aligned} \tag{3.5}$$

A comparison between the two theories has been made in Figure 3.14. It can be said that Creager and Paris's estimation for σ_y is close to the Irwin's modification that considers the plastic effects to the point of the estimated maximum stress. After that, they disagree since Creager and Paris solution doesn't consider plasticity. For σ_x, the consideration of blunting is needed since the experimental data of σ_x is way bellow σ_y. For calculating σ_y and σ_x , Creager and Paris (1967) Equations 3.5 has been used at $\theta = 0$ and (r) starts from $\frac{\rho}{2}$ according to the theory. For our samples, the crack tip radius was measured using a digital

microscope and the value was found to be about 60 μm.

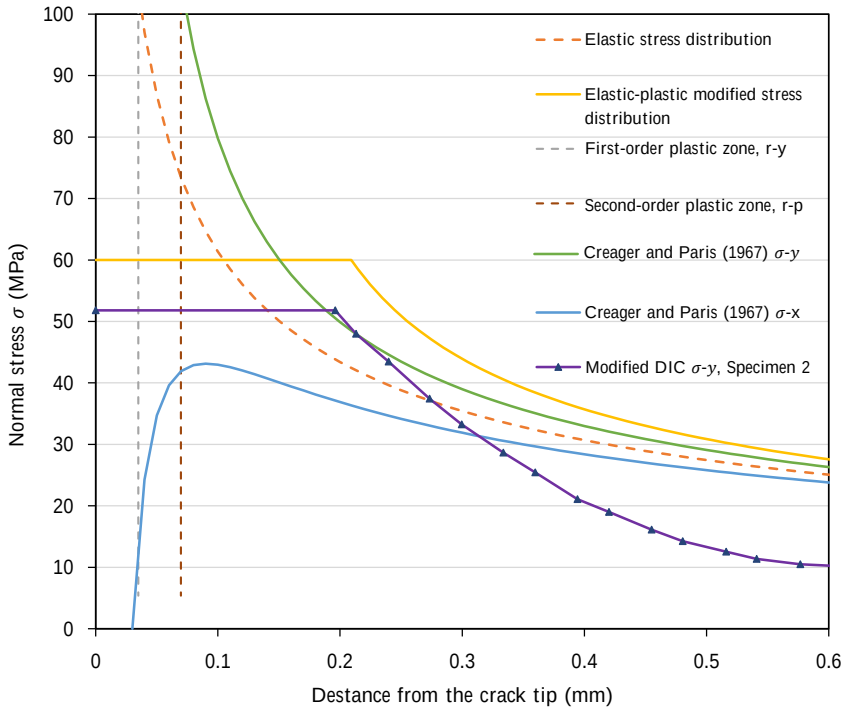

Figure 3.14: Comparison between Irwin's modification and Creager and Paris's estimation.

3.3.2 Stress Distribution for Diffident Samples' Loading

The experimental stress distribution along the crack path has been studied for different loading until the fracture, as shown in Figure 3.15. It is obvious how the stress starts to concentrate near the crack tip while loading the spaceman until the fracture occurred. Duo to the way that the compact tension samples are loaded, a compressive stress is recorded after 9 mm from the crack tip, which also increases while loading the sample. 158N is the peak load before the fracture.

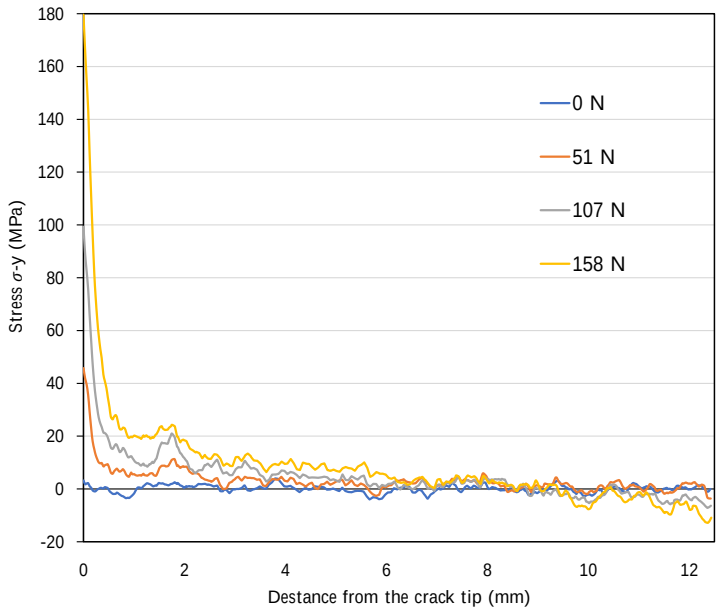

Figure 3.15: The normal stress σ_y distribution along the crack path for different loading.

3.3.3 Plastic Zone Shape

To estimate the plastic zone for all angles, an appropriate yield criterion has to be applied to the elastic stress field Equations 3.1. Considering the von Mises criterion 3.4 where σ_v is the von Mises stress, and σ_1,σ_2, and σ_3 are the three principal normal stress. Based on the Von Mises criterion, yielding occurs when σ_v=σ_{ys} and the principal stresses can be obtained from Mohr's circle relationship. Then, by substituting the Mode I stress fields into the principal stresses and then into the Von Mises Equation 3.4, solving for r_y will result in the estimate of Mode I plastic zone radius as a function of (θ) Equation 3.6.

$$r_y(\theta) = \frac{1}{4\pi}\left(\frac{K_I}{\sigma_{ys}}\right)^2\left[1+\cos\theta+\frac{3}{2}\sin^2\theta\right] \tag{3.6}$$

Figure 3.16 shows the significant difference in size and shape of the plastic zones between the plane stress and plane strain conditions. The estimates of Mode I plastic zone radius

as a function of (θ) and shown in Figure 3.16 are not fully correct because they are based on the purely elastic analysis, and the redistribution of the stress has not been taken into account. Even the Irwin plasticity correction is not totally correct [6, 33]. Figure 3.17 shows a comparison between the plane strain plastic zone shape estimated from Eq.3.6 with the elastic-plastic crack tip stress field obtained from finite element simulation, where n characterizes the strain hardening rate of material, and α is a dimensionless factor. The stress distribution associated with the simulation seems to be tilted to the side a little from the plastic zone shape estimated from the equation.

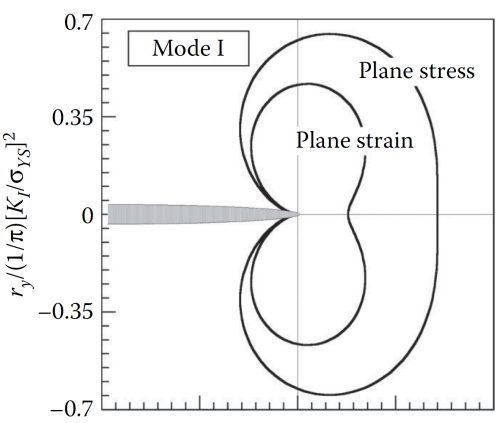

Figure 3.16: The plastic zone shape estimation from the elastic solution for Mode I. Obtained from [6].

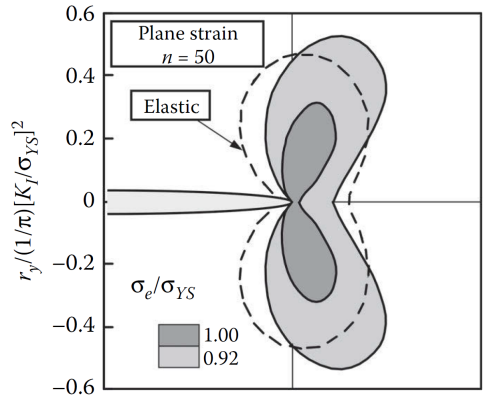

Figure 3.17: The effective stress from a finite element analysis Vs the plastic zone estimation [6].

Digital image correlation (DIC) allows us to visualize the strain distribution around the crack, which will give an idea of what shape the strain and stress are distributed. As it can be seen in Figure 3.18, the normal strain in the y-direction are also tilted to the opposite side of the crack, which matches the finite element analysis of the effective stress in Figure 3.17. As discussed before, the estimation of the plastic shape was not totally correct because it was based on an elastic analysis.

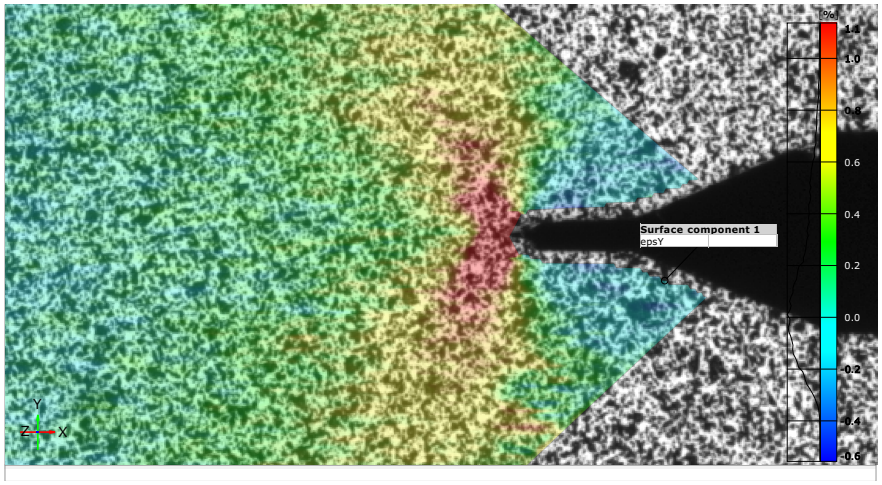

Figure 3.18: Strain distribution of y-direction.

Chapter 4: Conclusion

4.1 Summary and Conclusion

This research investigated the effects of Graphene Nanoplatelet (xGnP) on the fracture toughness of EPON 862 and SC-15. In two weight ratios, the xGnP was dispersed into the two epoxy resins: 0.1wt% and 0.5wt%. For the sake of comparison, nano-silica particles were added to EBPN 862. The fracture toughness of the baseline and reinforced resins was investigated with the compact tension (CT) experiment.

It was observed that xGnP resulted in a greater improvement in the fracture toughness of EPON 862 than that of SC-15. For EPON 862, the G_{IC} value was 412, 772, 1058 J/m^2 for the baseline, 0.1wt% and 0.5wt% reinforced, respectively, representing an improvement of 87% and 156%. The K_{IC} value was 1.0, 1.45, 1.71 $MPa.\sqrt{m}$ for the baseline, 0.1wt% and 0.5wt% reinforced, respectively, representing an improvement of 45% and 70%. For SC-15, the G_{IC} value was 965, 1168, 1106 J/m^2 for the baseline, 0.1wt% and 0.5wt% reinforced, representing an improvement of 21% and 14%. The KIC value was 1.54, 1.68, 1.58 $MPa.\sqrt{m}$ for the baseline, 0.1wt% and 0.5wt% reinforced, representing an improvement of 8.8% and 2.6%. The addition of xGnP led to marginal improvement at 0.1wt%. This effect started to diminish at 0.5wt%. The different effect of xGnP between the two epoxies is assumed to be because SC-15 is already rubber toughened. For comparison, EPON 862 was also reinforced with 80 nm diameter nano-silica particles. At 0.1wt% and 0.5wt%, the improvement in G_{IC} was 49% and 87%, respectively and the improvement in K_{IC} was 30% and 34%. It can be said that nano-silica improved the G_{IC} by $\sim$ 50% and K_{IC} by $\sim$ 64% of the enhancement obtained by adding xGnP for both weight fractions.

To conclude, adding xGnP will greatly increase the fracture toughness of a fairly brittle epoxy system. xGnP is found to be much more efficient than nano-silica at a low concentration. The method of introducing the pre-crack was found to have a major impact on the measurement of fracture toughness value in compact tension (CT) experiments. The residual strain fields resulting from pre-cracking procedure were analyzed using the Digital Image Correlation (DIC) method, and the corresponding residual stress fields were calculated. It was observed that the pre-cracking procedure that leaves high compressive residual stresses at the crack tip result in an increased fracture toughness value.

4.2 Future Work

The following important step would be fractography, which is the microscopic observation of the fracture surfaces, for interpreting the fracture mechanisms that occurred in the tested specimen. The next milestone would be testing the enforced epoxies with fiber-reinforced polymer (FRP) composites along with employing other composite enforcement methods such as a quasi-three-dimensional (Q3D) braided fiber. The investigation could include quantifying the enhancement caused by the two methods to Mode-I and Mode-II interlaminar fracture toughness and impact resistance.

APPENDIX

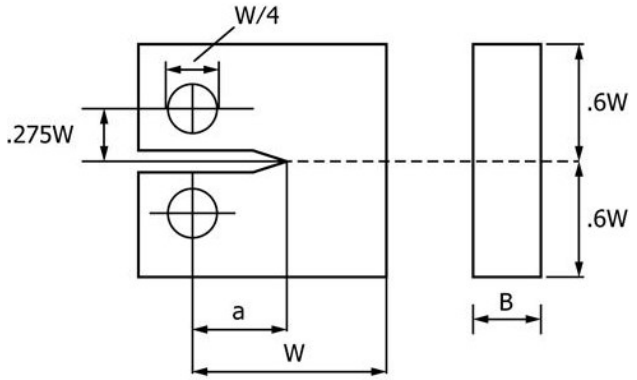

Figure A.1: Compact tension specimen configuration.

Table A.1: SC-15 Samples - baseline.

	Sample 1	Sample 2	Sample 3	Sample 4	Sample 5
W (mm)	23.95	24.09	24	23.98	24.03
a (mm)	11.15	11.17	11.13	11.16	11.12
B (mm)	6.25	6.35	6.24	5.88	5.9
P_Q (N)	176	173	173	156	166
K_{IC} $(MPa.\sqrt{m})$	1.59	1.52	1.55	1.49	1.56
G_{IC} (J/m^2)	992	1023	984	894	930

Table A.2: SC-15 Samples - 0.1wt% xGnP.

	Sample 1	Sample 2	Sample 3	Sample 4	Sample 5	Sample 6	Sample 7
W (mm)	24	23.65	24.34	23.78	23.74	23.85	23.83
a (mm)	11.12	11.095	11.184	11.104	11.106	1.114	1.109
B (mm)	6	6.21	6.29	5.84	5.82	5.65	5.45
P_Q (N)	173	196	184	174	172	159	162
K_{IC} $(MPa.\sqrt{m})$	1.63	1.77	1.74	1.68	1.67	1.60	1.68
G_{IC} (J/m^2)	1144	1382	1176	1097	1013	1087	1276

Table A.3: SC-15 Samples - 0.5wt% xGnP.

	Sample 1	Sample 2	Sample 3	Sample 4	Sample 5	Sample 6	Sample 7
W (mm)	24	23.9	23.8	23.9	23.92	24.2	23.7
a (mm)	11.38	11.33	11.15	11.15	11.131	11.48	11.06
B (mm)	6.15	6.15	6.05	6.2	5.9	6.04	5.83
P_Q (N)	170	181	169	180	158	161	153
K_{IC} $(MPa.\sqrt{m})$	1.516	1.71	1.59	1.64	1.54	1.53	1.55
G_{IC} (J/m^2)	1175	1178	1194	1109	1101	946	1037

Table A.4: EPON 862 Samples - baseline.

	Sample 1	Sample 2	Sample 3	Sample 4	Sample 5	Sample 6	Sample 7	Sample 8
W (mm)	24	24.05	24	24	24	24.05	24.1	24
a (mm)	11	11.2	11.5	11.03	11.1	1.105	1.106	11.5
B (mm)	5.95	6	5.8	6.47	6.03	6.7	6.17	6.03
P_Q (N)	92	81	64	143	142	147	148	72
K_{IC} ($MPa.\sqrt{m}$)	0.85	0.76	0.65	1.22	1.31	1.21	1.31	0.7
G_{IC} (J/m^2)	254	197	169	481	651	631	729	183

Table A.5: EPON 862 Samples - 0.1wt% xGnP.

	Sample 1	Sample 2	Sample 3	Sample 4	Sample 5
W (mm)	24.05	24	24.08	24.15	24.4
a (mm)	11.21	11.24	11.28	11.35	11.3
B (mm)	5.83	5.6	5.7	5.64	5.7
P_Q (N)	148	146	147	138	159
K_{IC} ($MPa.\sqrt{m}$)	1.43	1.47	1.44	1.4	1.54
G_{IC} (J/m^2)	994	821	719	666	862

Table A.6: EPON 862 Samples - 0.5wt% xGnP.

	Sample 1	Sample 2	Sample 3	Sample 4	Sample 5
W (mm)	24.3	24.2	24.2	24.55	24.2
a (mm)	11.64	11.5	11.59	11.83	11.59
B (mm)	5.95	6.14	6.2	6.06	6.1
P_Q (N)	189	177	190	170	185
K_{IC} ($MPa.\sqrt{m}$)	1.85	1.66	1.78	1.64	1.62
G_{IC} (J/m^2)	1121	1041	1094	995	1038

Table A.7: EPON 862 Samples - 0.1wt% Nano-Silica.

	Sample 1	Sample 2	Sample 3	Sample 4	Sample 5
W (mm)	24.2	24.2	24.39	24.14	24.1
a (mm)	11.39	11.4	11.18	11.24	11.21
B (mm)	6.14	6.17	6.06	6.1	6.2
P_Q (N)	146	128	140	154	145
K_{IC} ($MPa.\sqrt{m}$)	1.35	1.18	1.31	1.41	1.31
G_{IC} (J/m^2)	742	536	600	659	530

Table A.8: EPON 862 Samples - 0.5wt% Nano-Silica.

	Sample 1	Sample 2	Sample 3	Sample 4
W (mm)	24.09	24.3	24.58	24.6
a (mm)	11.45	11.52	12	11.51
B (mm)	5.82	5.85	5.36	5.61
P_Q (N)	135	152	130	151
K_{IC} $(MPa.\sqrt{m})$	1.34	1.48	1.44	1.50
G_{IC} (J/m^2)	635	727	798	914

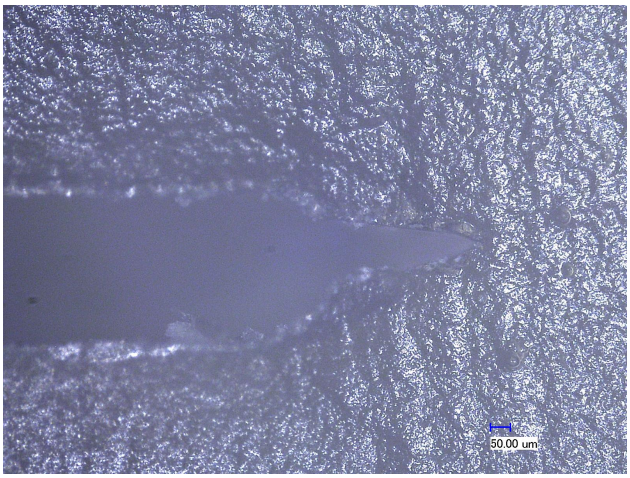

Figure A.2: Microscopic image of a crack tip made by razor sliding.

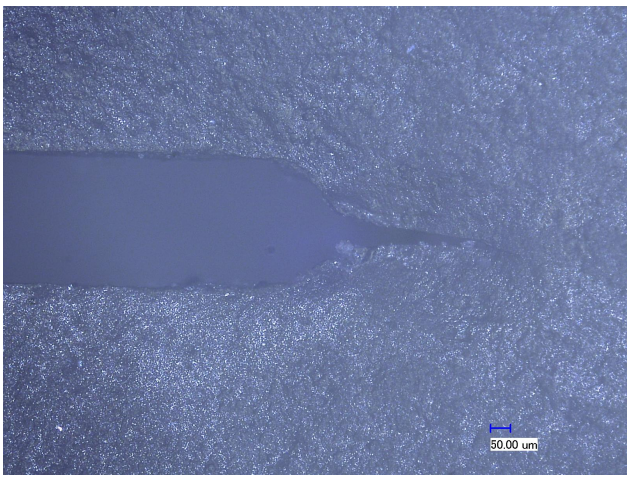

Figure A.3: Microscopic image of a crack tip made by razor pressing.

BIBLIOGRAPHY

BIBLIOGRAPHY

[1] D. L. Hunston, R. J. Moulton, N. J. Johnston, and W. Bascom, "Matrix resin effects in composite delamination: mode i fracture aspects," in *Toughened composites*, ASTM International, 1987.

[2] N. Domun, H. Hadavinia, T. Zhang, T. Sainsbury, G. Liaghat, and S. Vahid, "Improving the fracture toughness and the strength of epoxy using nanomaterials–a review of the current status," *Nanoscale*, vol. 7, no. 23, pp. 10294–10329, 2015.

[3] E. Preiß, "Fracture toughness of freestanding metallic thin films studied by bulge testing," 2018.

[4] T. L. Anderson and T. L. Anderson, *Fracture mechanics: fundamentals and applications*. CRC press, 2005.

[5] ASTM International, "D5045-14 Standard Test Methods for Plane-Strain Fracture Toughness and Strain Energy Release Rate of Plastic Materials," standard, ASTM International, West Conshohocken, PA, 2014.

[6] T. L. Anderson, *Fracture mechanics: fundamentals and applications*. CRC press, 2017.

[7] W. J. Cantwell and J. Morton, "The impact resistance of composite materials—a review," *composites*, vol. 22, no. 5, pp. 347–362, 1991.

[8] M. Richardson and M. Wisheart, "Review of low-velocity impact properties of composite materials," *Composites Part A: Applied Science and Manufacturing*, vol. 27, no. 12, pp. 1123–1131, 1996.

[9] N. Sela and O. Ishai, "Interlaminar fracture toughness and toughening of laminated composite materials: a review," *Composites*, vol. 20, no. 5, pp. 423–435, 1989.

[10] V. Dikshit, S. K. Bhudolia, and S. C. Joshi, "Multiscale polymer composites: A review of the interlaminar fracture toughness improvement," *Fibers*, vol. 5, no. 4, p. 38, 2017.

[11] Y. Tang, L. Ye, Z. Zhang, and K. Friedrich, "Interlaminar fracture toughness and cai strength of fibre-reinforced composites with nanoparticles–a review," *Composites Science and Technology*, vol. 86, pp. 26–37, 2013.

[12] M. A. Rafiee, J. Rafiee, Z. Wang, H. Song, Z.-Z. Yu, and N. Koratkar, "Enhanced mechanical properties of nanocomposites at low graphene content," *ACS nano*, vol. 3, no. 12, pp. 3884–3890, 2009.

[13] R. J. Young, I. A. Kinloch, L. Gong, and K. S. Novoselov, "The mechanics of graphene nanocomposites: a review," *Composites Science and Technology*, vol. 72, no. 12, pp. 1459–1476, 2012.

[14] C. Lee, X. Wei, J. W. Kysar, and J. Hone, "Measurement of the elastic properties and intrinsic strength of monolayer graphene," *science*, vol. 321, no. 5887, pp. 385–388, 2008.

[15] A. Kumar, *Multiscale characterization and modeling of progressive failure in nanographene reinforced carbon/epoxy composites*. PhD thesis, University of Alabama Libraries, 2016.

[16] M. A. Rafiee, "Graphene-based composite materials," *Rensselaer Polytechnic Institute: Troy, NY, USA*, 2011.

[17] A. S. Wajid, H. T. Ahmed, S. Das, F. Irin, A. F. Jankowski, and M. J. Green, "High-performance pristine graphene/epoxy composites with enhanced mechanical and electrical properties," *Macromolecular Materials and engineering*, vol. 298, no. 3, pp. 339–347, 2013.

[18] A. Kumar, S. Li, S. Roy, J. A. King, and G. M. Odegard, "Fracture properties of nanographene reinforced epon 862 thermoset polymer system," *Composites Science and Technology*, vol. 114, pp. 87–93, 2015.

[19] A. Kumar and S. Roy, "Characterization of mixed mode fracture properties of nanographene reinforced epoxy and mode i delamination of its carbon fiber composite," *Composites Part B: Engineering*, vol. 134, pp. 98–105, 2018.

[20] Y. Yang, W. Rigdon, X. Huang, and X. Li, "Enhancing graphene reinforcing potential in composites by hydrogen passivation induced dispersion," *Scientific reports*, vol. 3, p. 2086, 2013.

[21] A. A. Griffith, "Vi. the phenomena of rupture and flow in solids," *Philosophical transactions of the royal society of london. Series A, containing papers of a mathematical or physical character*, vol. 221, no. 582-593, pp. 163–198, 1921.

[22] C. E. Inglis, "Stresses in a plate due to the presence of cracks and sharp corners," *Trans Inst Naval Archit*, vol. 55, pp. 219–241, 1913.

[23] G. R. Irwin, "Onset of fast crack propagation in high strength steel and aluminum alloys," tech. rep., Naval Research Lab Washington DC, 1956.

[24] H. M. Westergaard, "Bearing pressures and cracks," *Trans AIME, J. Appl. Mech.*, vol. 6, pp. 49–53, 1939.

[25] G. R. Irwin, "Analysis of stresses and strains near the end of a crack transversing a plate," *Trans. ASME, Ser. E, J. Appl. Mech.*, vol. 24, pp. 361–364, 1957.

[26] A. Wells, "Unstable crack propagation in metals: cleavage and fast fracture," in *Proceedings of the crack propagation symposium*, vol. 1, 1961.

[27] J. R. Rice, "A path independent integral and the approximate analysis of strain concentration by notches and cracks," 1968.

[28] X. G. Sciences, "(xGnP) Graphene Nanoplatelets - Grade C." https://xgsciences.com/product/xgnp/, April 2020.

[29] I. M. McAninch, J. J. La Scala, G. R. Palmese, and E. J. Robinette, "Thin film initiation of cracks for fracture toughness measurements in epoxy resins," *Journal of Applied Polymer Science*, vol. 134, no. 1, 2017.

[30] G. E. Dieter and D. Bacon, *Mechanical metallurgy*, vol. 3. McGraw-hill New York, 1986.

[31] R. W. Hertzberg and F. E. Hauser, *Deformation and fracture mechanics of engineering materials*. 1977.

[32] M. Creager and P. C. Paris, "Elastic field equations for blunt cracks with reference to stress corrosion cracking," *International journal of fracture mechanics*, vol. 3, no. 4, pp. 247–252, 1967.

[33] P. Kumar and K. Prashant, *Elements of fracture mechanics*. Tata McGraw-Hill Education, 2009.